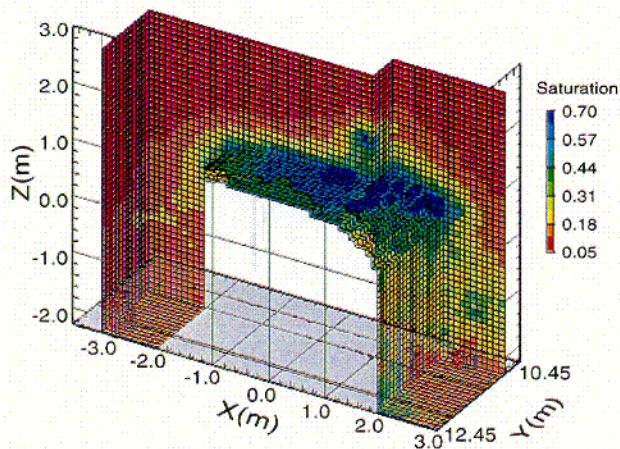
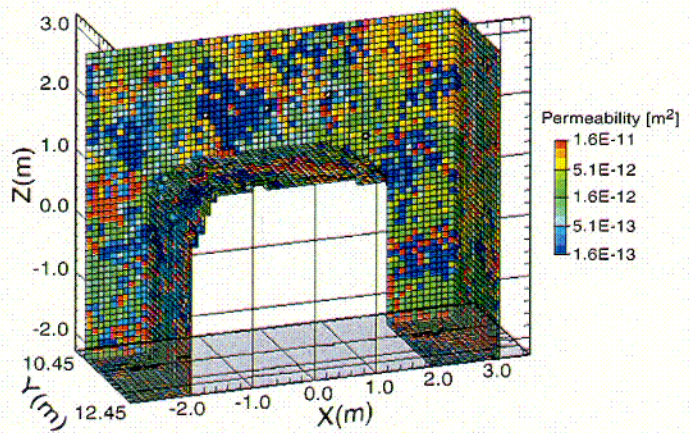


154_0031.ai

154_0031.ai

Figure 4.2-1. Seepage-Relevant Features and Processes



154_0008.ai

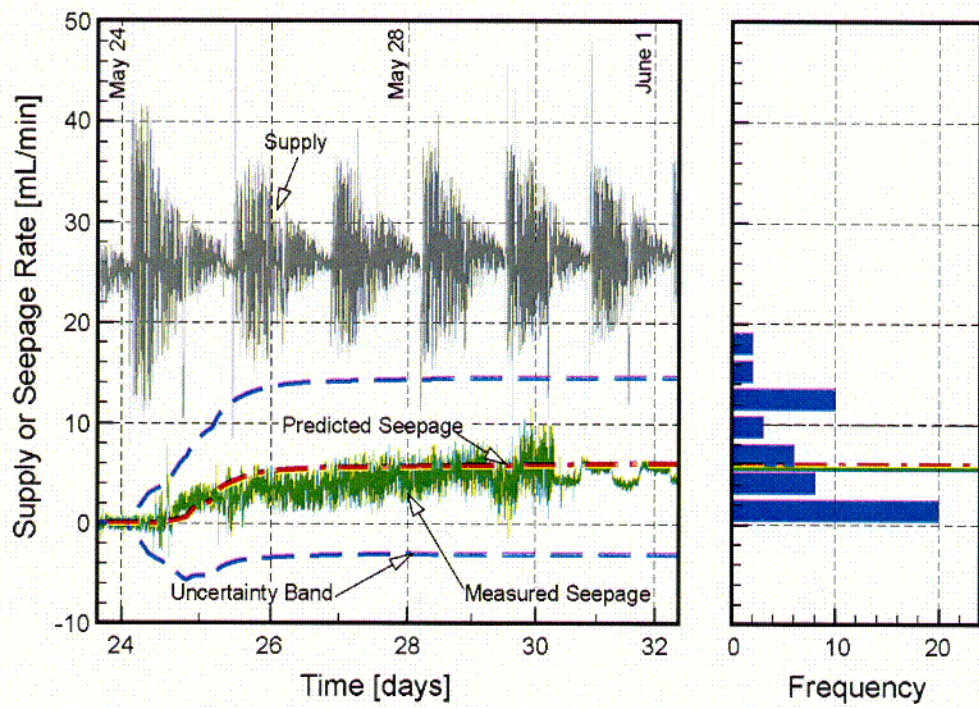
154_0008.ai

Source: CRWMS M&O 2001 [DIRS 153045], Figures 11 and 12c.

NOTE: Permeability field (upper) and late-time saturation distribution (lower) for a simulated liquid release test in Exploratory Studies Facility Niche 4 (located at stations 47 and 88).

Figure 4.3.1-1. Permeability and Saturation for a Simulated Liquid Release

CO2



154_0009.ai

154_0009.ai

Source: CRWMS M&O 2001 [DIRS 153045], Figure 7c.

NOTE: Seepage experiments conducted in Zone 1 of borehole SYBT-ECRB-LA#2. The simulation uncertainty is calculated using first-order second-moment uncertainty propagation analysis. The right panel shows the histogram of the seepage rate at the end of the experiment as predicted by Monte Carlo simulations. Time is days since 00:00, April 30, 2000.

Figure 4.3.1-2. Water Supply, Measured Seepage Rates, and Predicted Seepage Rates



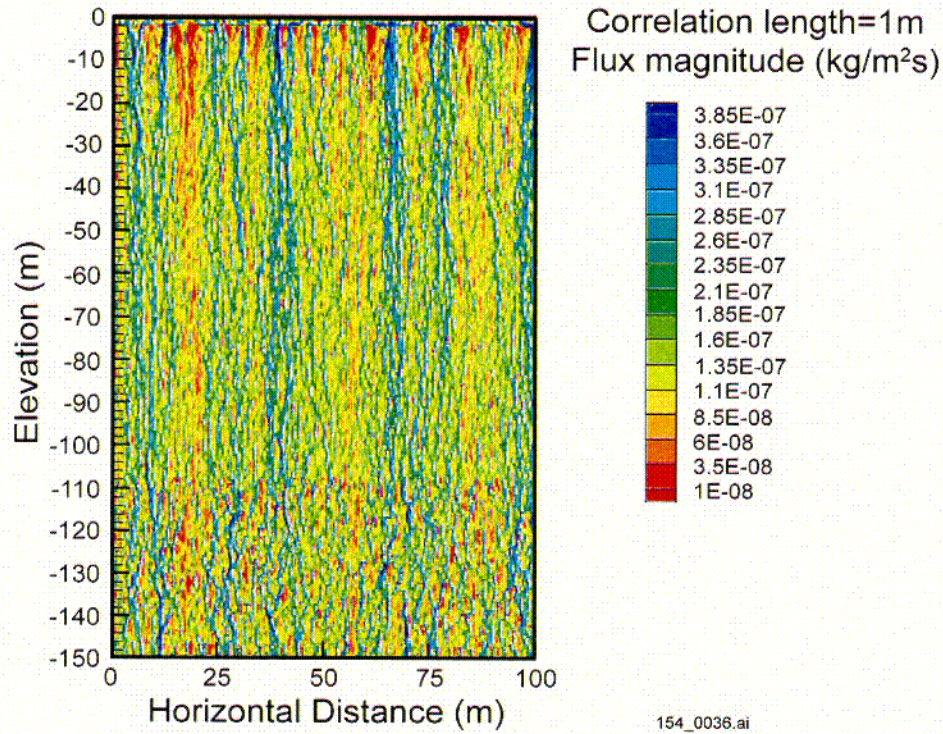
154_0010a.ai

154_0010a.ai

NOTE: Photo shows spallation (see arrow) of vertical plaster wall, but no effect to plastered ceiling. The line between the zigzag pattern and the leaf pattern separates the ceiling from the wall.

Figure 4.3.1-3. Tomb of Sennefer in the Egyptian Valley of the Kings

COY



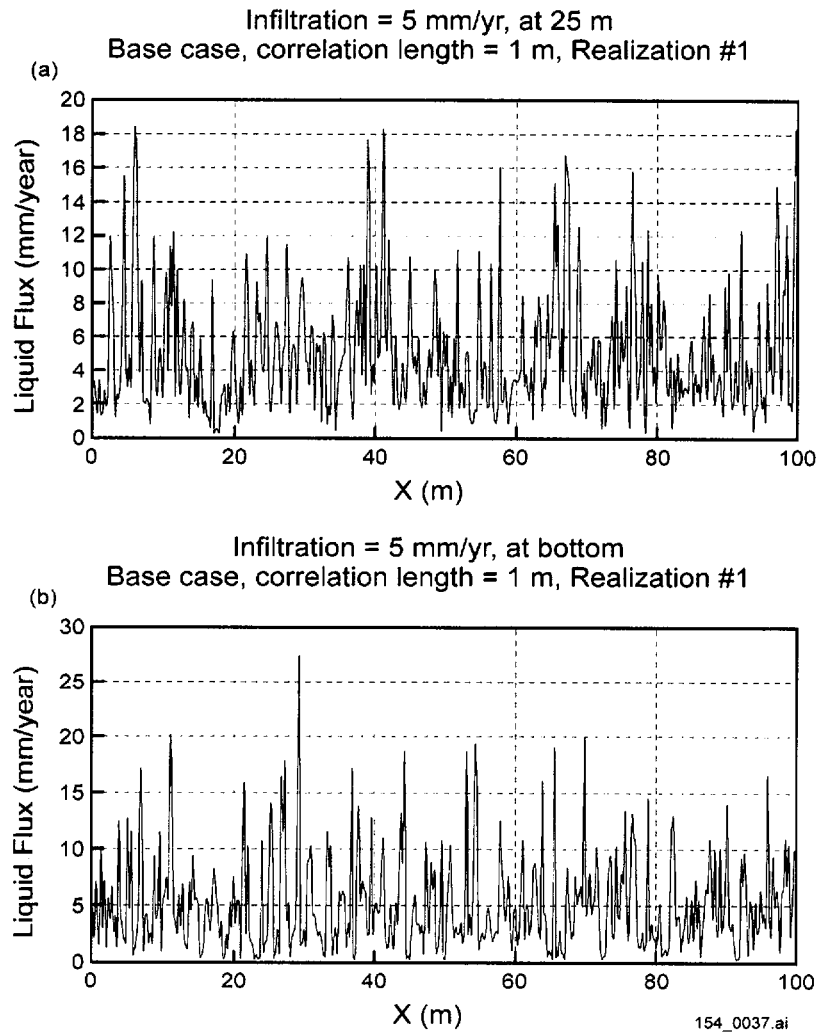
154_0036.ai

Source: Bodvarsson 2001 [DIRS 154669], Attachment 16, data file listed on p. 11.

NOTE: Simulation using the base case scenario with 1-m correlation length, forming several high-flux flow paths.

Figure 4.3.2-1. Distribution of Flux Magnitude within the Two-Dimensional Model Domain

CO5

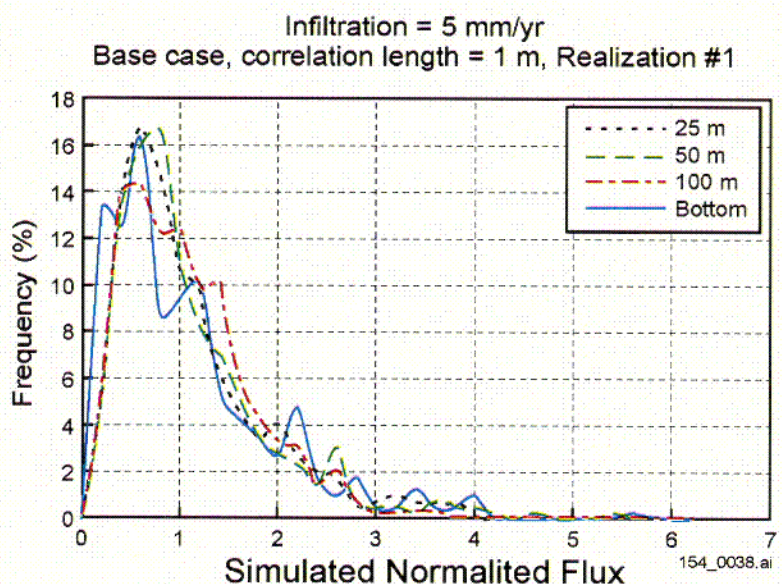


154_0037.ai

Source: Bodvarsson 2001 [DIRS 154669], Attachment 16, p. 12 and data files listed on p. 11.

NOTE: Simulated using the base case scenario, correlation length = 1 m, infiltration = 5 mm/yr, (a) at a depth of 25 m or (b) at the bottom.

Figure 4.3.2-2. Distribution of Vertical Fluxes within the Two-Dimensional Model Domain



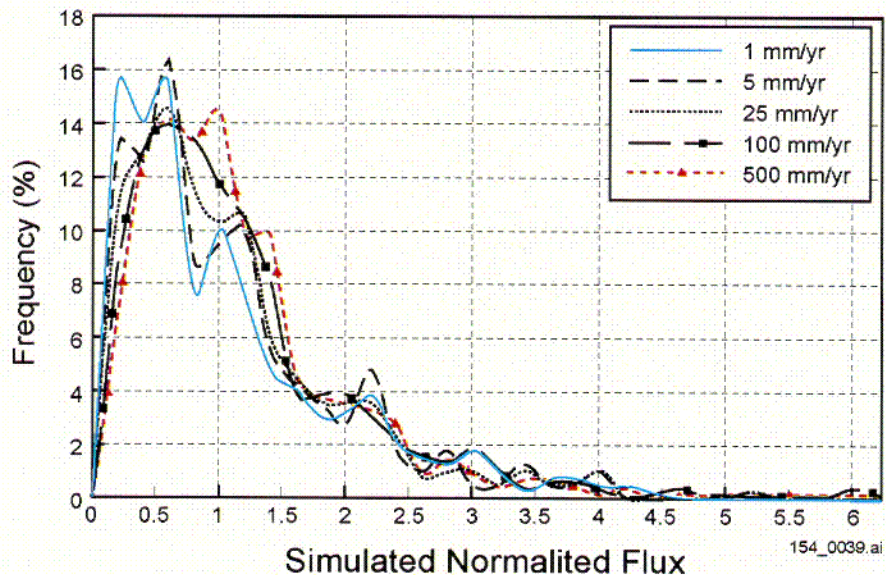
154_0038.ai

Source: Bodvarsson 2001 [DIRS 154669], Attachment 16, p. 13.

NOTE: Simulated using the base case scenario, correlation length = 1 m, infiltration = 5 mm/yr, and Realization #1.

Figure 4.3.2-3. Comparison of Frequency Distribution of Simulated Fluxes at Different Elevations within the Two-Dimensional Model Domain

Code



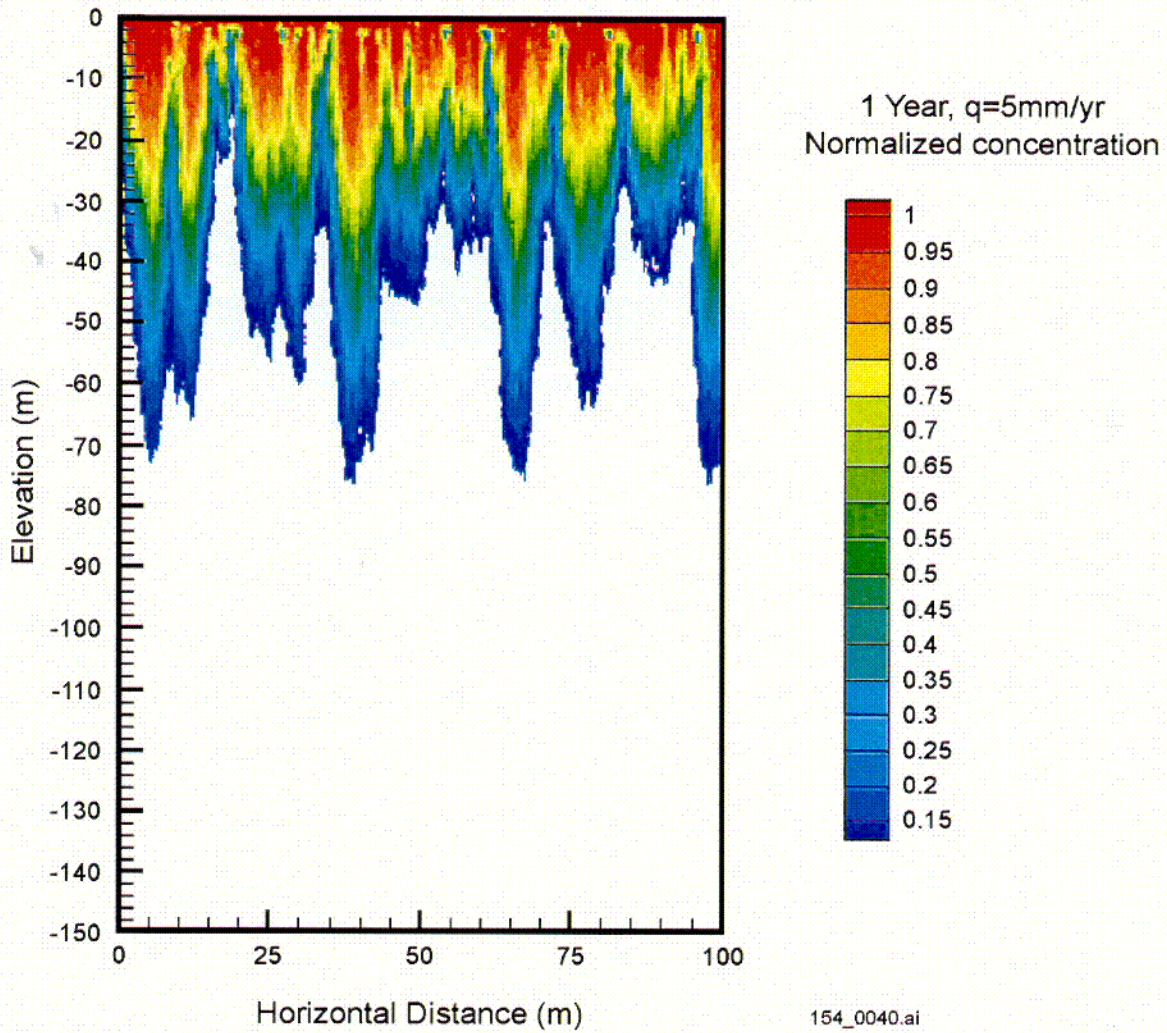
154_0039.ai

Source: Bodvarsson 2001 [DIRS 154669], Attachment 16, p. 14.

NOTE: Simulated with Realization #1, flux at potential repository horizon.

Figure 4.3.2-4. Frequency Distribution of Simulated Fluxes at Different Infiltration Rates within the Two-Dimensional Model Domain

COT



154_0040.ai

Source: Bodvarsson 2001 [DIRS 154669], Attachment 16, p. 20.

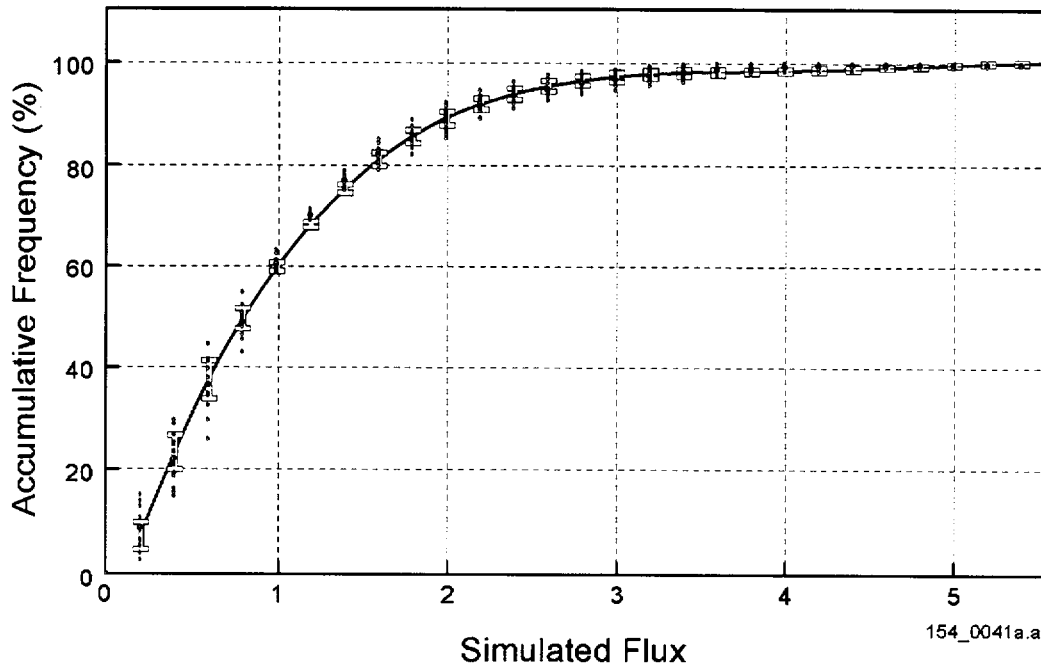
NOTE: Simulated distribution of tracer concentration within the model domain; simulation time = 1 yr, $q = 5 \text{ mm/yr}$.

Figure 4.3.2-5. Simulated Preferential Flow Pathways

Co8

Bottom flux distribution (with 95% confidence range)

$$y = -0.3137x^4 + 5.4998x^3 - 35.66x^2 + 102.3x - 11.434$$

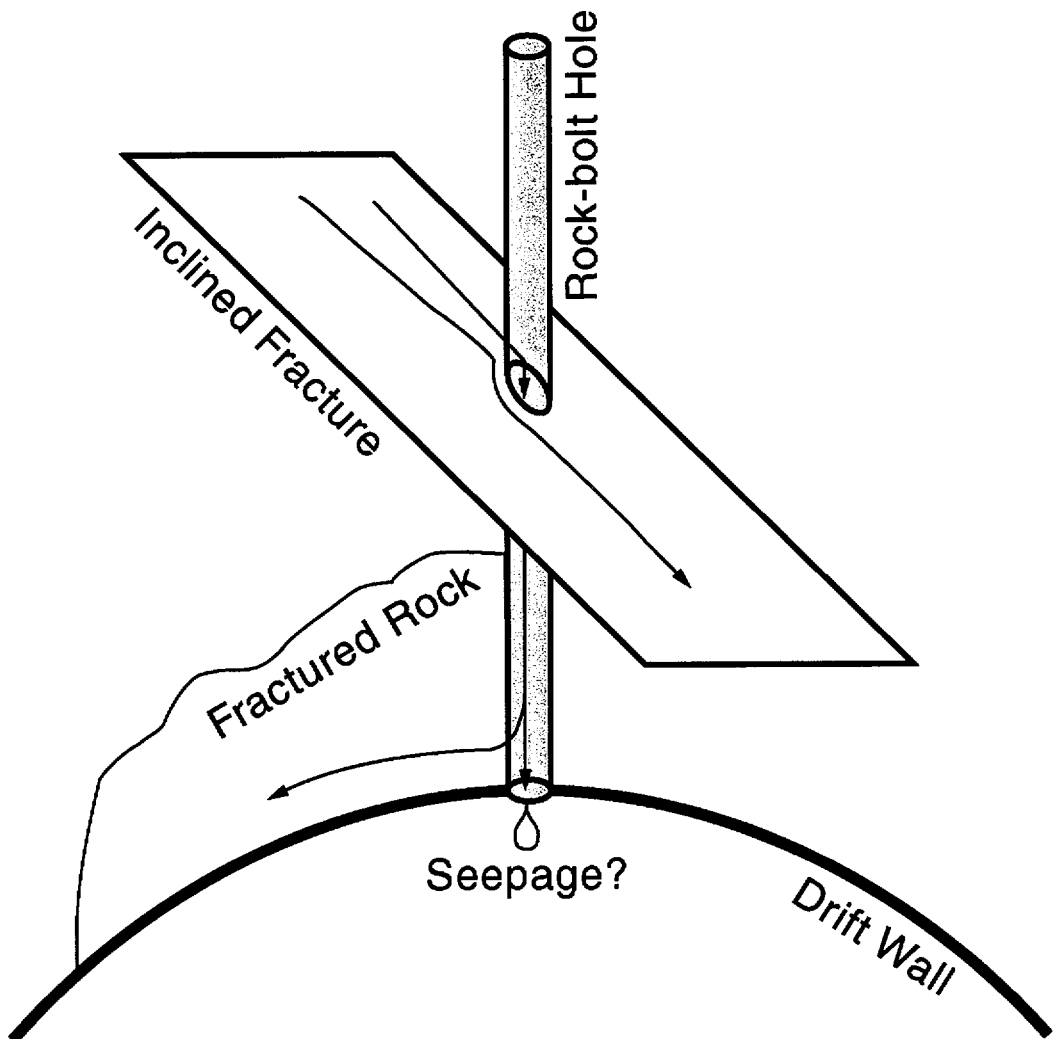


154_0041a.ai

Source: Bodvarsson 2001 [DIRS 154669], Attachment 16, p. 22.

NOTE: Results averaged over all simulations. Regression: $y = -0.3137x^4 + 5.4998x^3 - 35.66x^2 + 102.3x - 11.434$. Range is given as the 95-percent confidence interval.

Figure 4.3.2-6. Distribution and Range of Cumulative Flux as a Function of Percolation Flux for the Bottom of the Model Domain

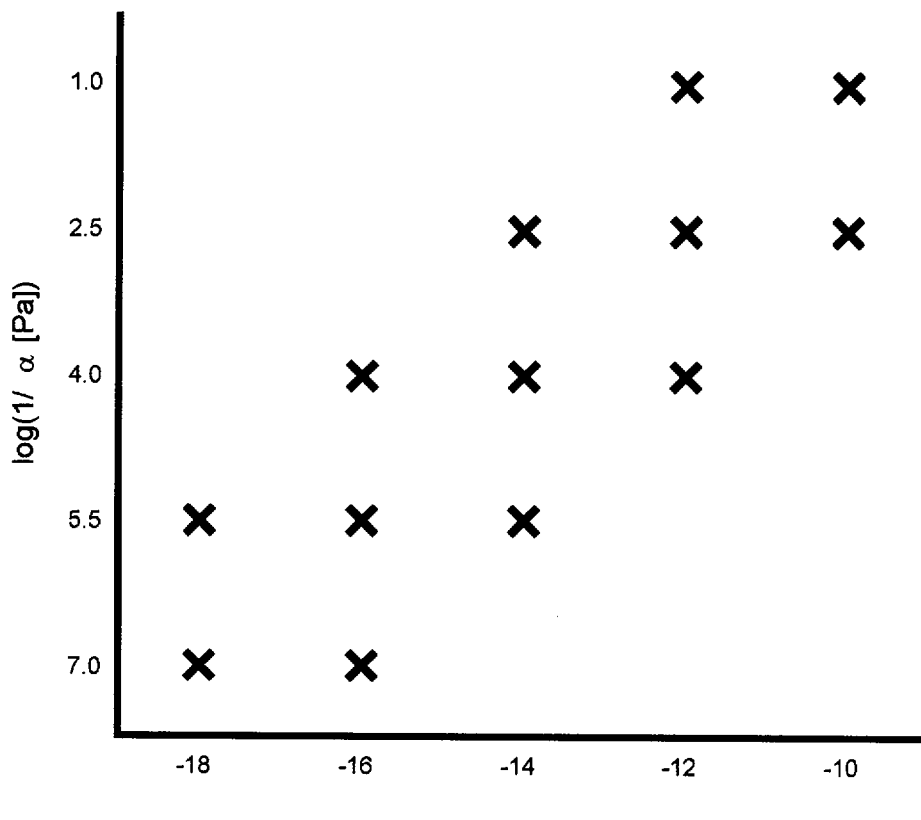


154_0015a.ai

154_0015a.ai

NOTE: Arrows show possible flow paths, which may result in seepage directly attributable to the presence of a rock bolt hole.

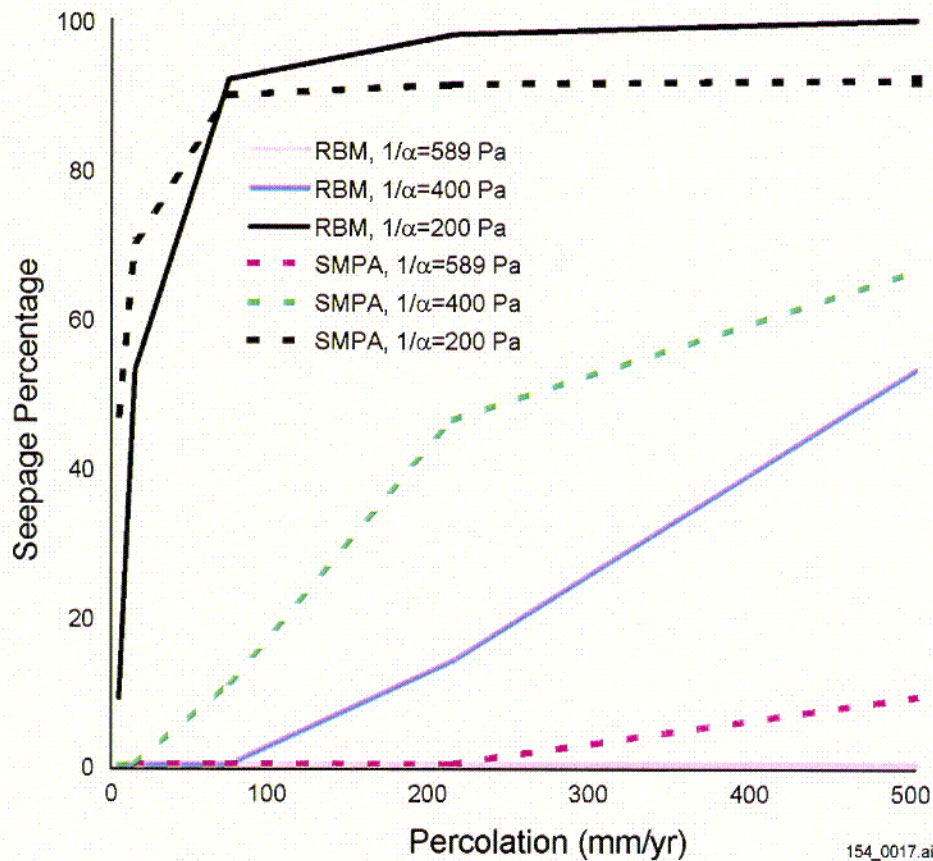
Figure 4.3.3-1. Conceptual Model of How a Rock Bolt Hole Might Affect Seepage



154_0016.ai

NOTE: Permeability is k and capillarity is $1/\alpha$.

Figure 4.3.3-2. Grout Parameter Combinations



154_0017.ai

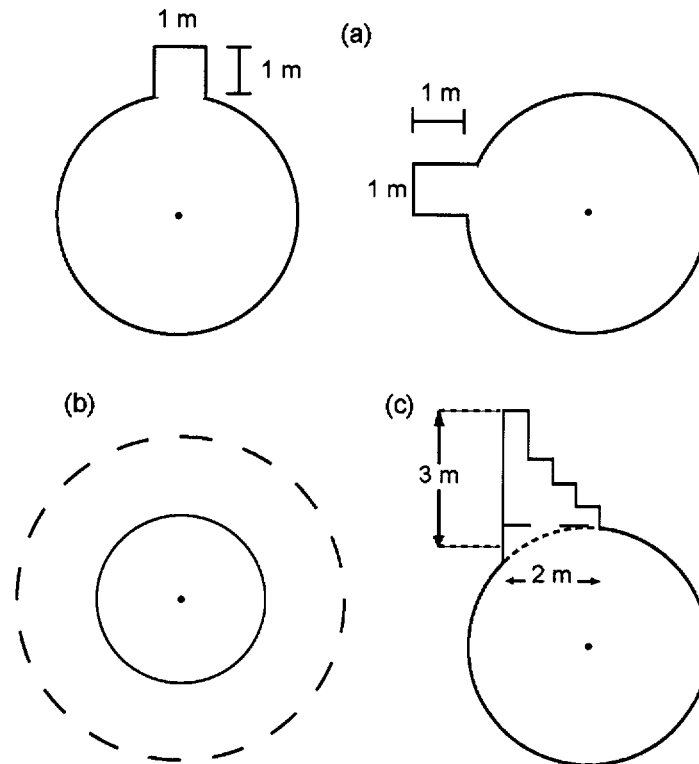
154_0017.ai

Source: DTN: LB0011SMDCREV1.002 [DIRS 153570]; TerBerg 2001 [DIRS 155102].

NOTE: Seepage percentage predicted by homogeneous rock bolt model (RBM) (without rock bolt) compared to that for the heterogeneous seepage model for performance assessment (SMPA) (CRWMS M&O 2000 [DIRS 148384], Section 6.3.1). For the cases with $1/\alpha$ equal to 200 and 400 Pa, the permeability is $0.9 \times 10^{-12} \text{ m}^2$ rather than $1.4 \times 10^{-12} \text{ m}^2$.

Figure 4.3.3-3. Comparison of Seepage Percentage

CD9

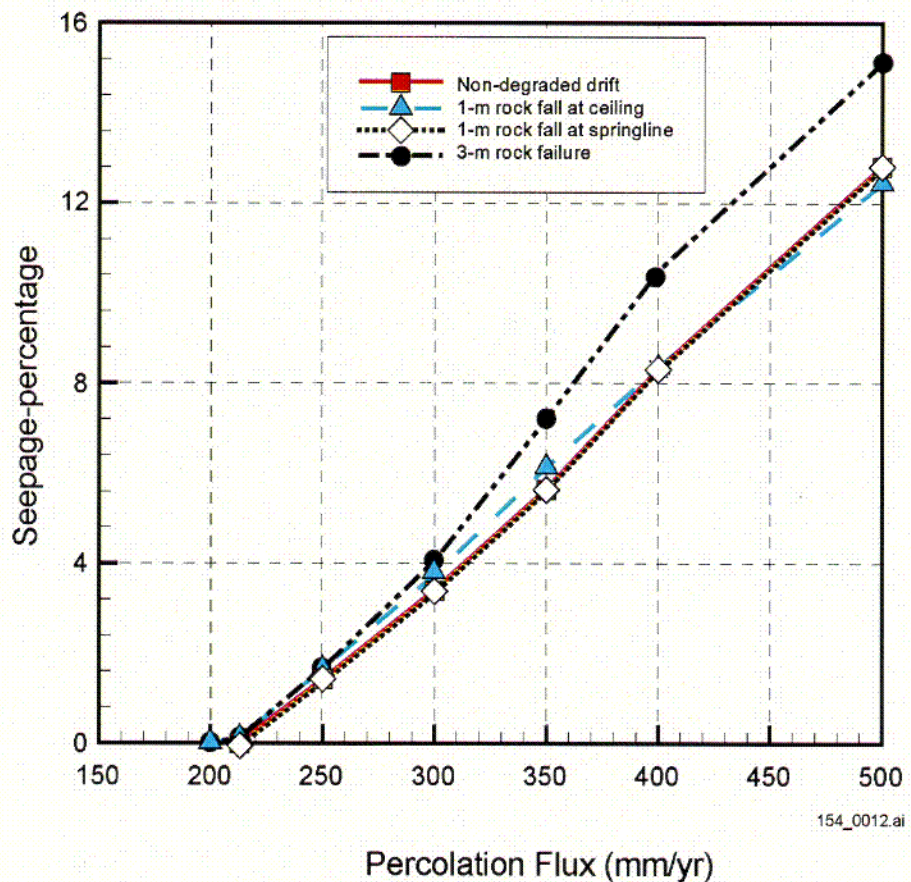


154_0011.ai

154_0011.ai

NOTE: Two cases of rockfall from the drift ceiling (upper panel), fracture dilation (lower left panel), and extended rock failure at the drift roof (lower right panel).

Figure 4.3.4-1. Drift Degradation Submodel Scenarios

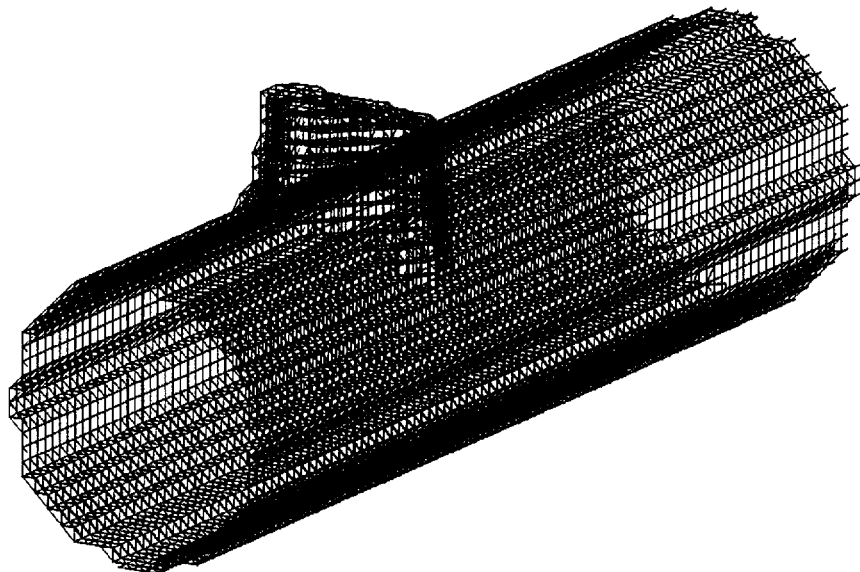


154_0012.ai

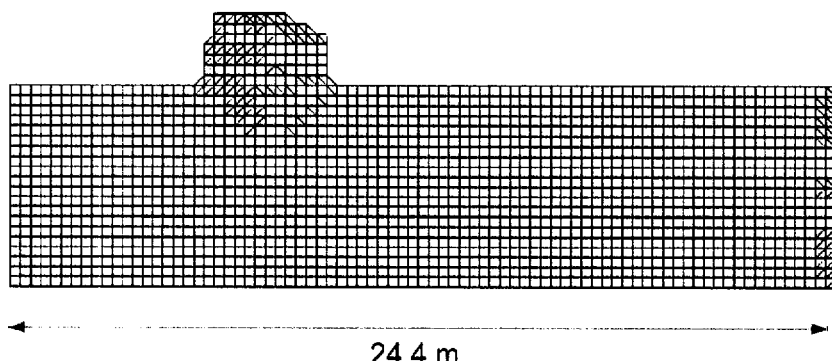
Source: DTN: LB0011SMDCREV1.002 [DIRS 153570], LB0011SMDCREV1.001 [DIRS 153574].

Figure 4.3.4-2. Seepage Percentage as a Function of Percolation Flux for the Three Set A Drift Degradation Scenarios

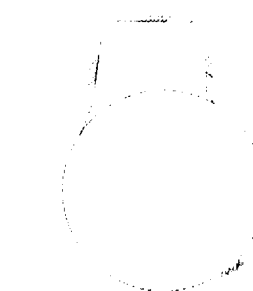
C10



(a) Isometric View



(b) Side View



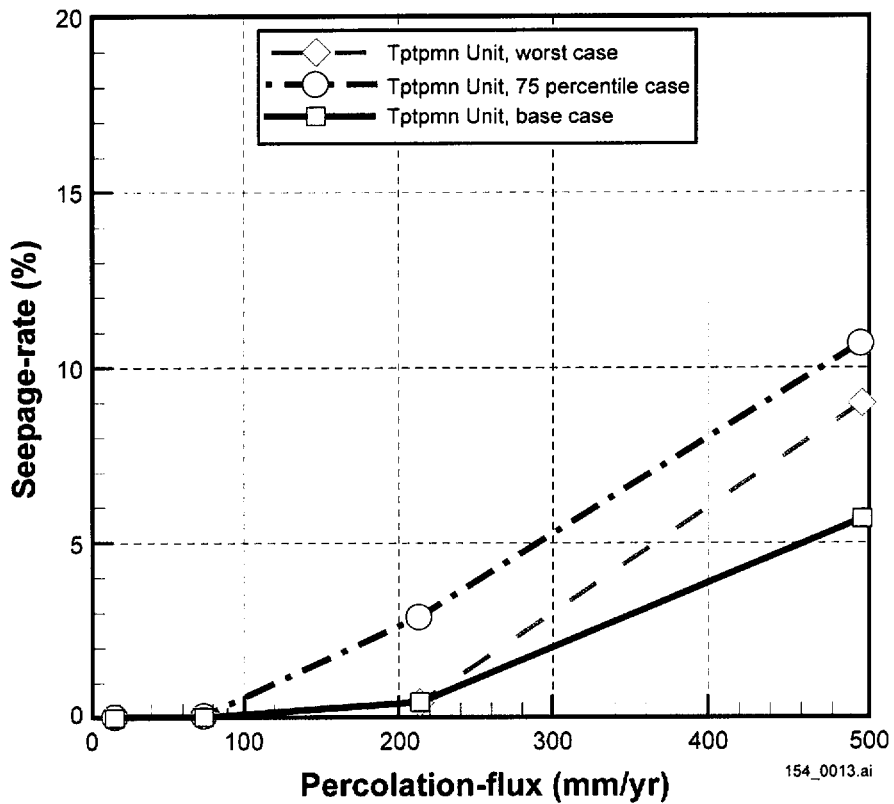
(c) Cross Section View

154_0018.ai

Source: DTN: MO0010RDDAAMRR.002 [DIRS 154048].

154_0018.ai

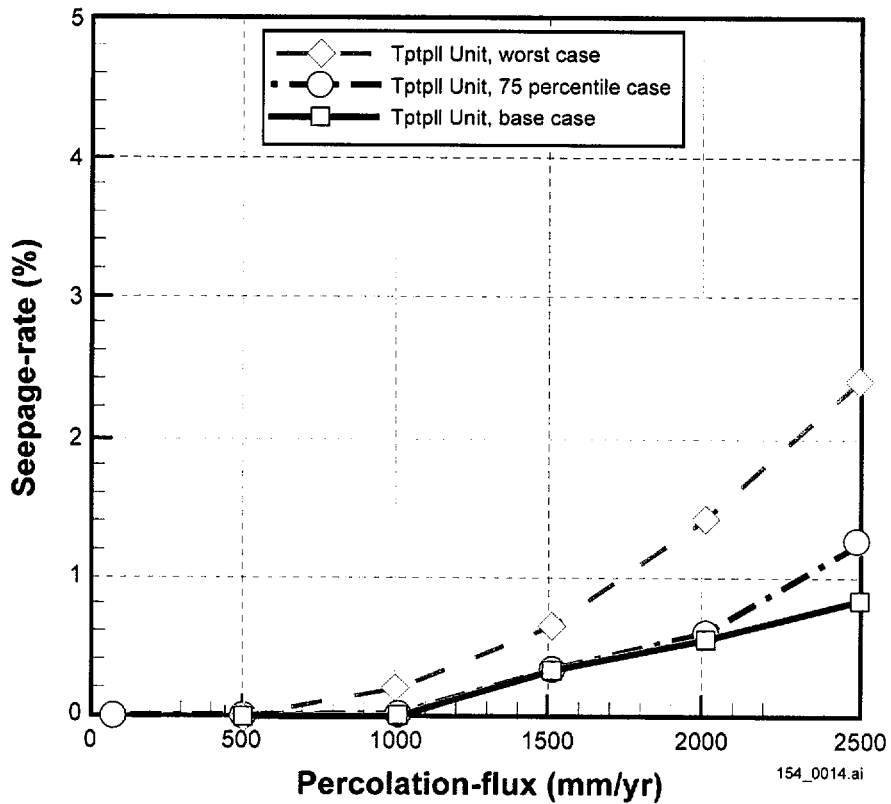
Figure 4.3.4-3. Emplacement Drift Profile for the Tptpmn Unit, Worst Case



154_0013.ai

Source: TerBerg 2001 [DIRS 155032].

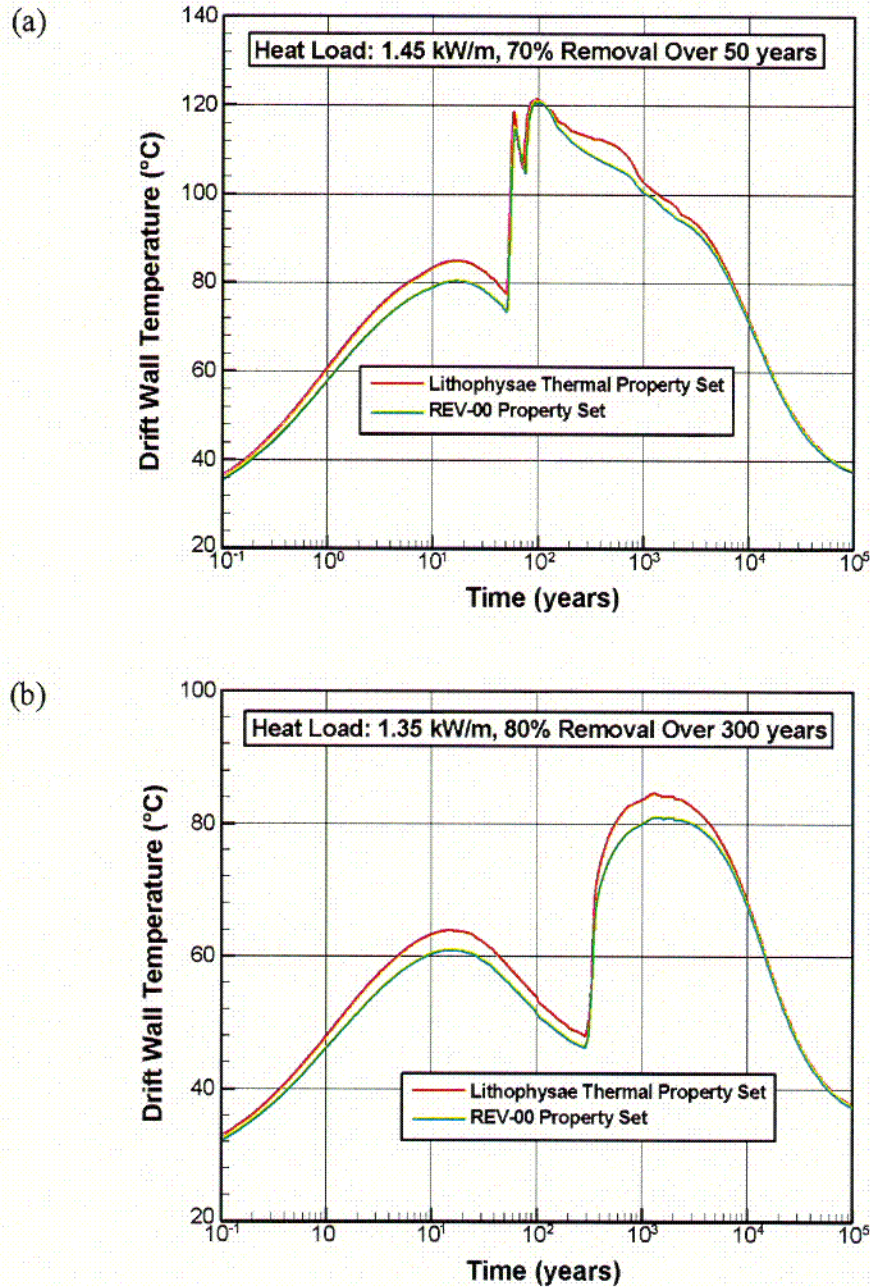
Figure 4.3.4-4. Seepage Percentage as a Function of Percolation Flux for Realization 1 of the Two Set A (Tptpmn) Degradation Scenarios and the Undegraded Base Case



154_0014.ai

Source: TerBerg 2001 [DIRS 155032].

Figure 4.3.4-5. Seepage Percentage as a Function of Percolation Flux for Realization 1 of the Two Set B' Degradation Scenarios and the Undegraded Base Case



154_0191.ai

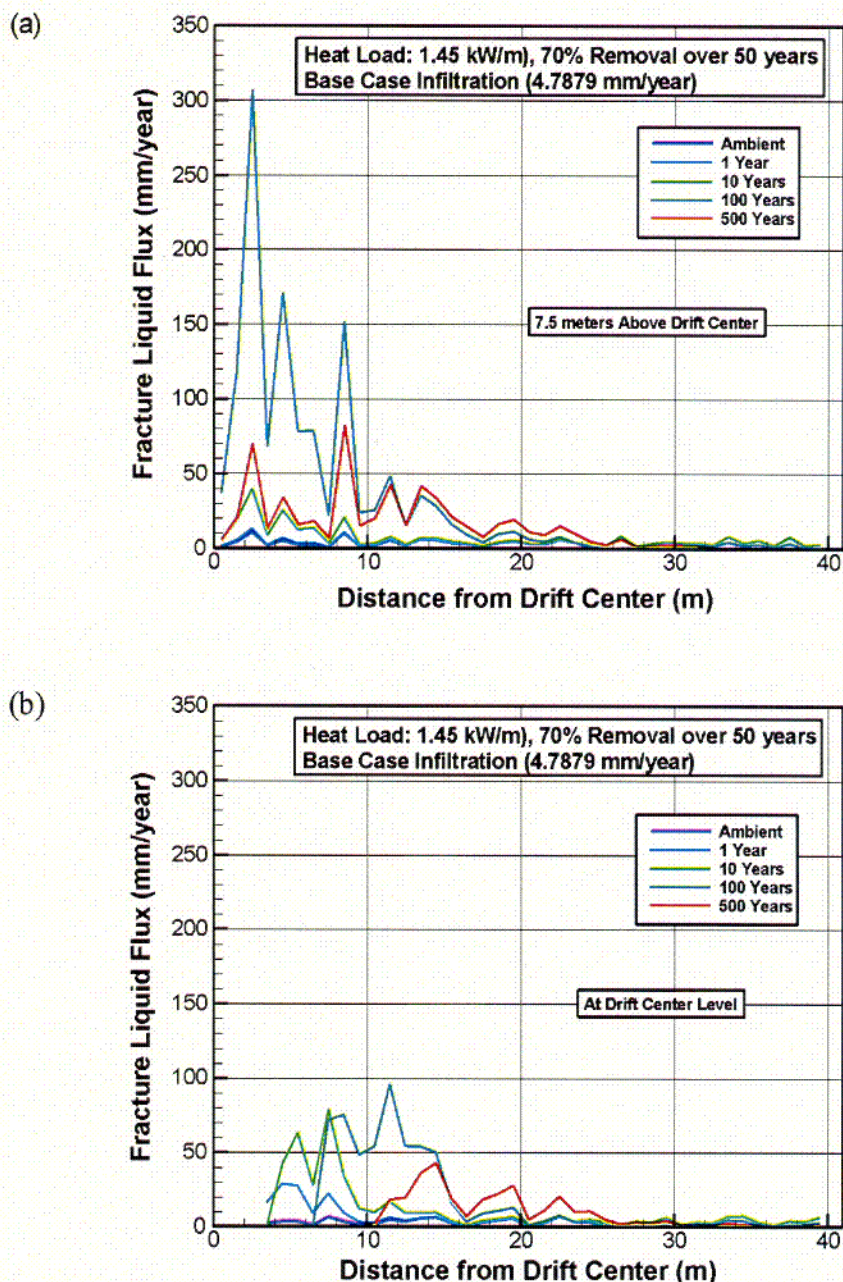
154_0191.ai

Source: Bodvarsson 2001 [DIRS 154669], Attachment 17, pp. 75 and 76. REV-00 refers to CRWMS M&O 2000 [DIRS 143665].

NOTE: Sensitivity of drift wall temperature to thermal properties (with and without the effects of lithophysal cavities) for (a) the higher-temperature case [heat load of 1.45 kW/m and ventilation of 70 percent over 50 years], and (b) the lower-temperature case [heat load of 1.35 kW/m and ventilation of 80 percent over 300 years].

Figure 4.3.5-1. Sensitivity of Drift Wall Temperature to Thermal Properties

CII



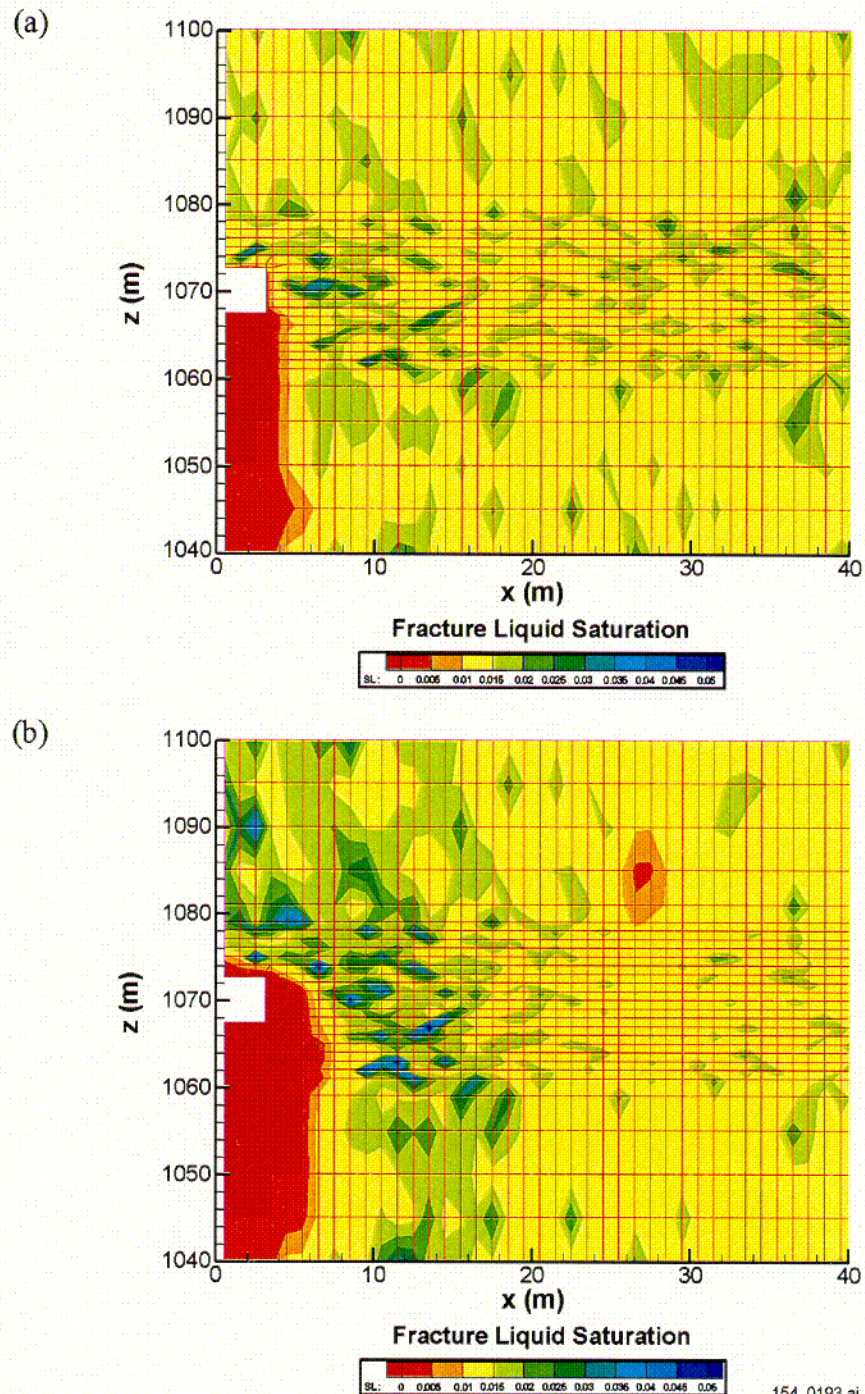
154_0192.ai

154_0192.ai

Source: Bodvarsson 2001 [DIRS 154669], Attachment 17, pp. 63 and 64.

NOTE: Fracture liquid fluxes for the higher-temperature case (heat load of 1.45 kW/m, ventilation of 70 percent over 50 yrs, and base case infiltration of 4.7879 mm/yr] at (a) a horizontal plane 7.5 m above drift center and (b) a horizontal plane along the drift center.

Figure 4.3.5-2. Fracture Liquid Fluxes as a Function of Lateral Distance from Drift Center



154_0193.ai

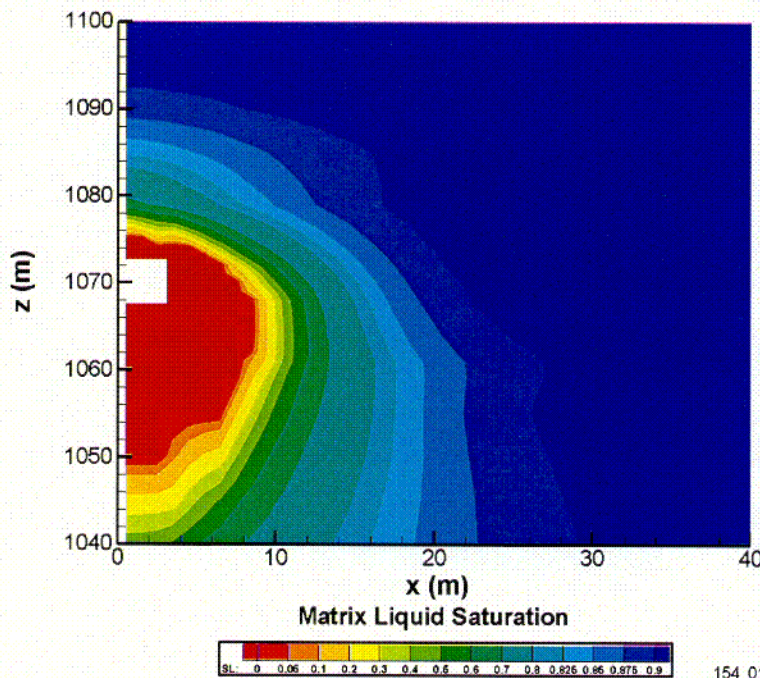
Source: Bodvarsson 2001 [DIRS 154669], Attachment 17, pp. 60 and 61.

NOTE: Higher-temperature operating mode at (a) 50 years after waste emplacement and (b) 100 years after waste emplacement.

154_0193.ai

Figure 4.3.5-3. Liquid Saturation Contours Around the Drift to Mid-Pillar

C13



154_0194.ai

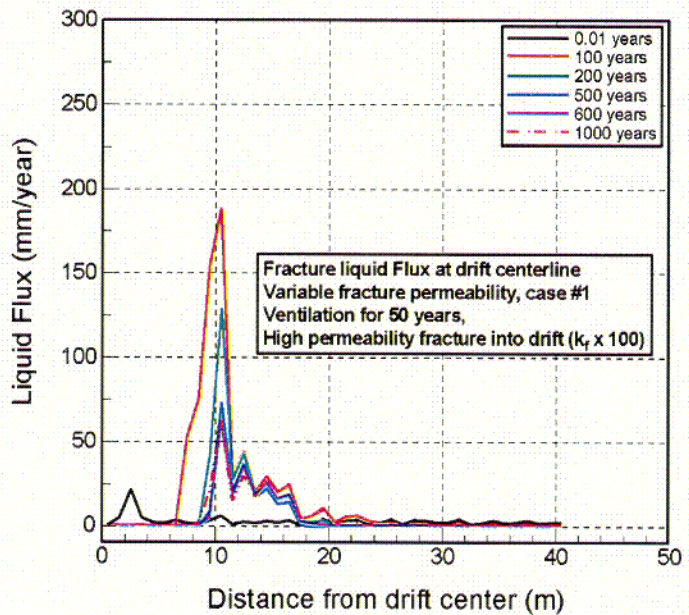
154_0194.ai

Source: Bodvarsson 2001 [DIRS 154669], Attachment 17, p. 62.

NOTE: Higher-temperature case; matrix permeability is homogeneous.

Figure 4.3.5-4. Matrix Liquid Saturations at 1,000 Years after Waste Emplacement

C14



154_0195.ai

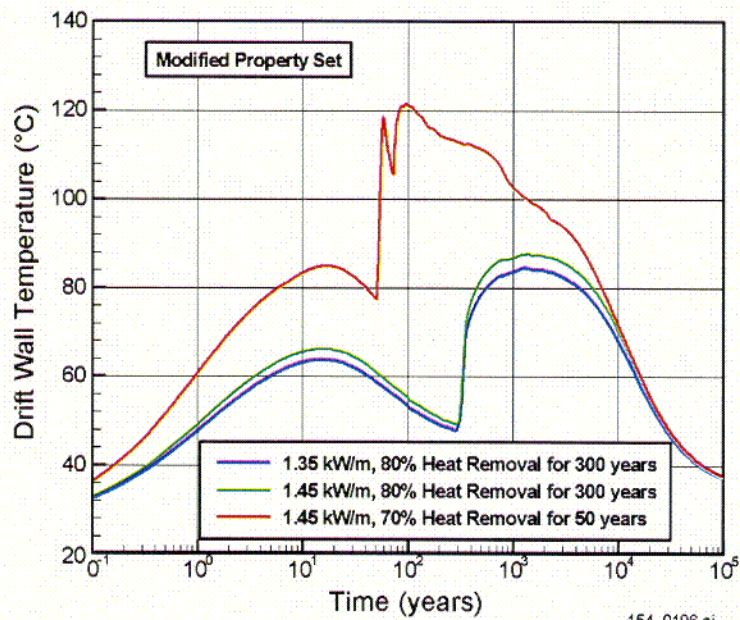
154_0195.ai

Source: Bodvarsson 2001 [DIRS 154669], Attachment 6, p. 46.

NOTE: Fracture liquid fluxes as a function of lateral distance from drift center, at a horizontal plane along the drift center for the higher-temperature case. These results are based on a heterogeneity field that has an artificially large permeability discrete feature intercepting the drift. Test conditions include fracture liquid flux at drift centerline, variable fracture permeability (Case 1), ventilation for 50 yrs, and high permeability fracture into drift ($k_f \times 100$).

Figure 4.3.5-5. Fracture Liquid Fluxes as a Function of Lateral Distance from Drift Center

C15



154_0196.ai

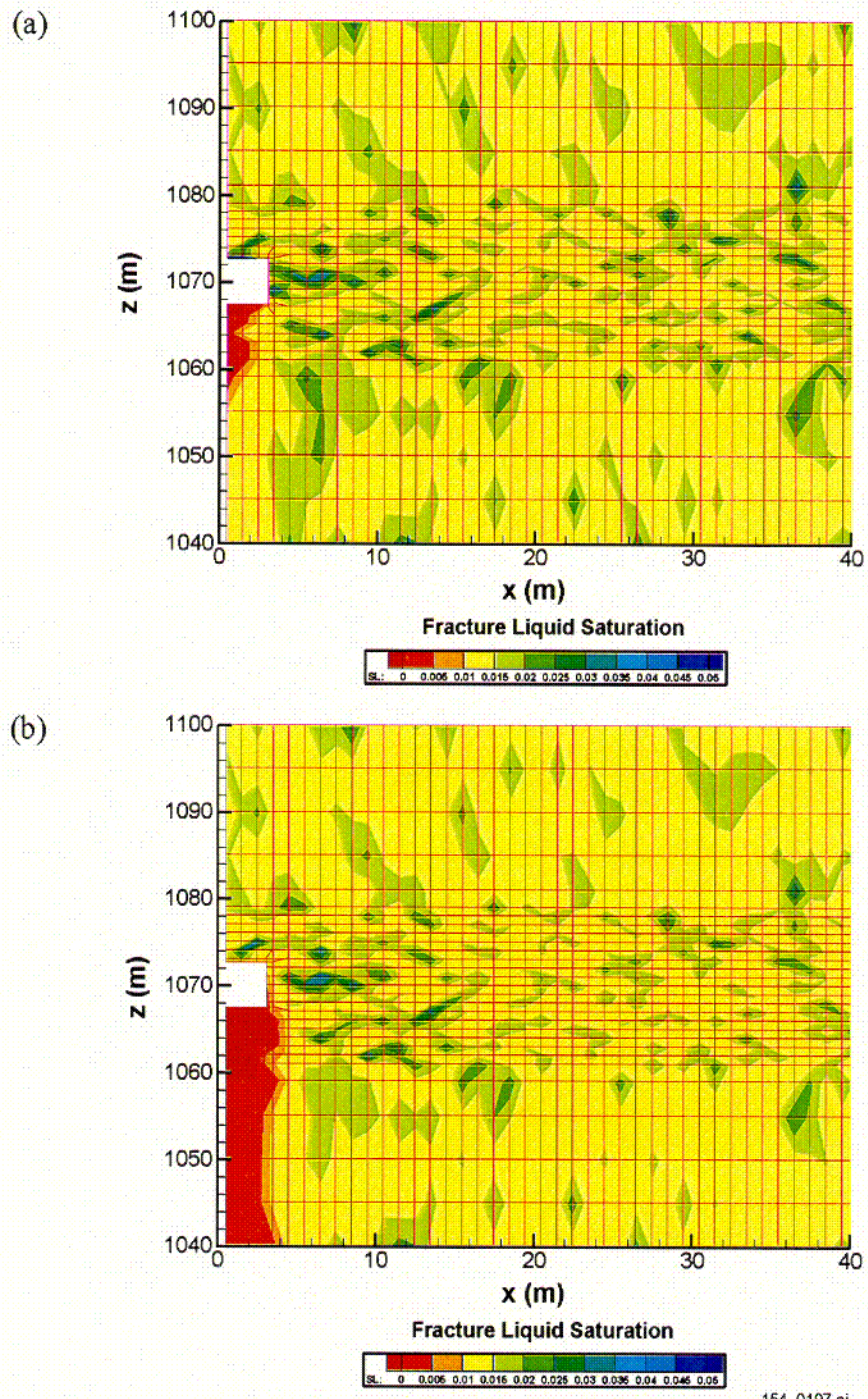
154_0196.ai

Source: Bodvarsson 2001 [DIRS 154669], Attachment 17, p. 74.

NOTE: Test conditions under the modified property set. Higher-temperature case = 1.45 kW/m, 70% heat removal for 50 years. Lower-temperature case = 1.35 kW/m, 80% heat removal for 300 years. Modified property set = high-permeability fracture into drift (as in Figure 4.3.5-5).

Figure 4.3.5-6. Comparison of Drift Wall Temperatures for the Higher-Temperature and Lower-Temperature Cases

C16

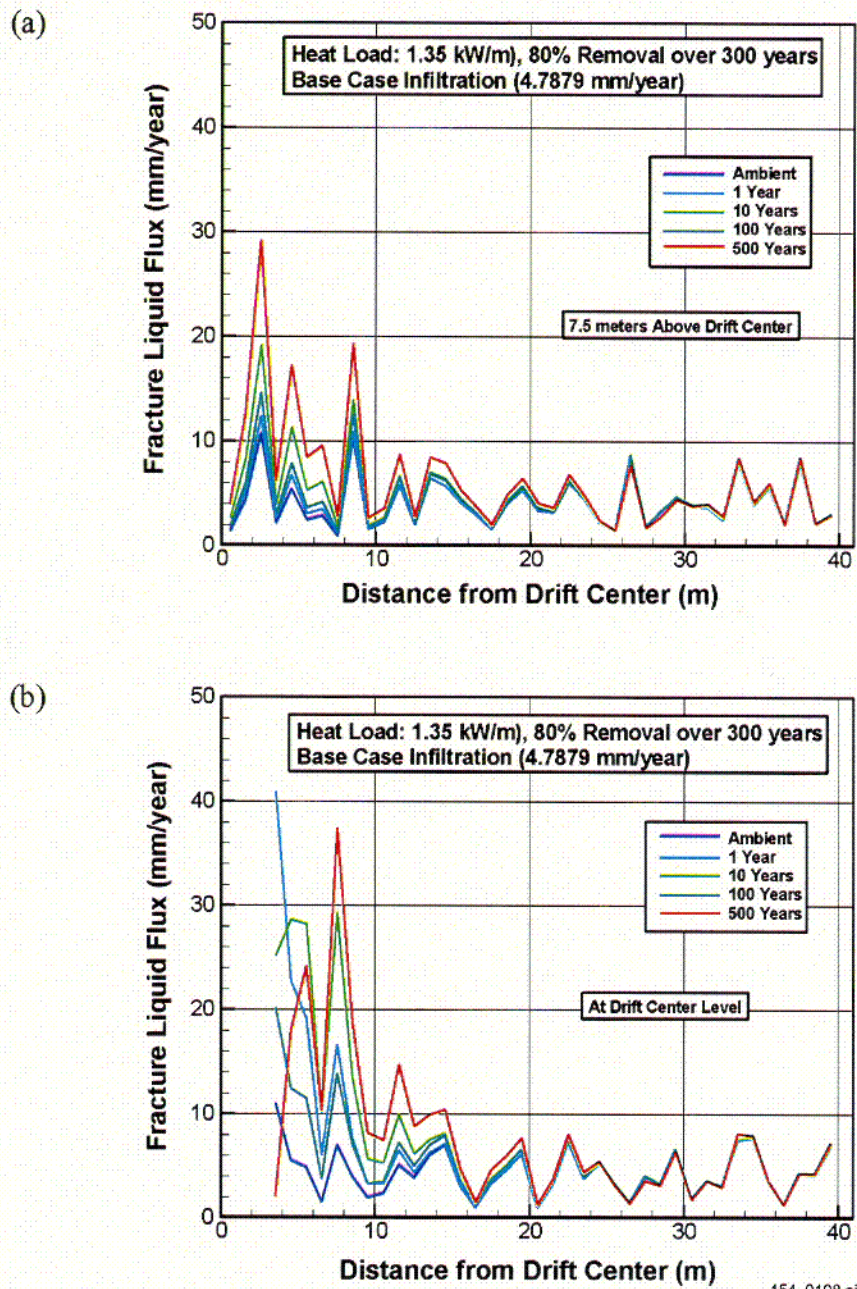


154_0197.ai

Source: Bodvarsson 2001 [DIRS 154669], Attachment 17, pp. 70 and 71.

NOTE: Fracture saturation contours at (a) 50 and (b) 500 years after waste emplacement.

Figure 4.3.5-7. Fracture Saturation Contours for the Lower-Temperature Case



154_0198.ai

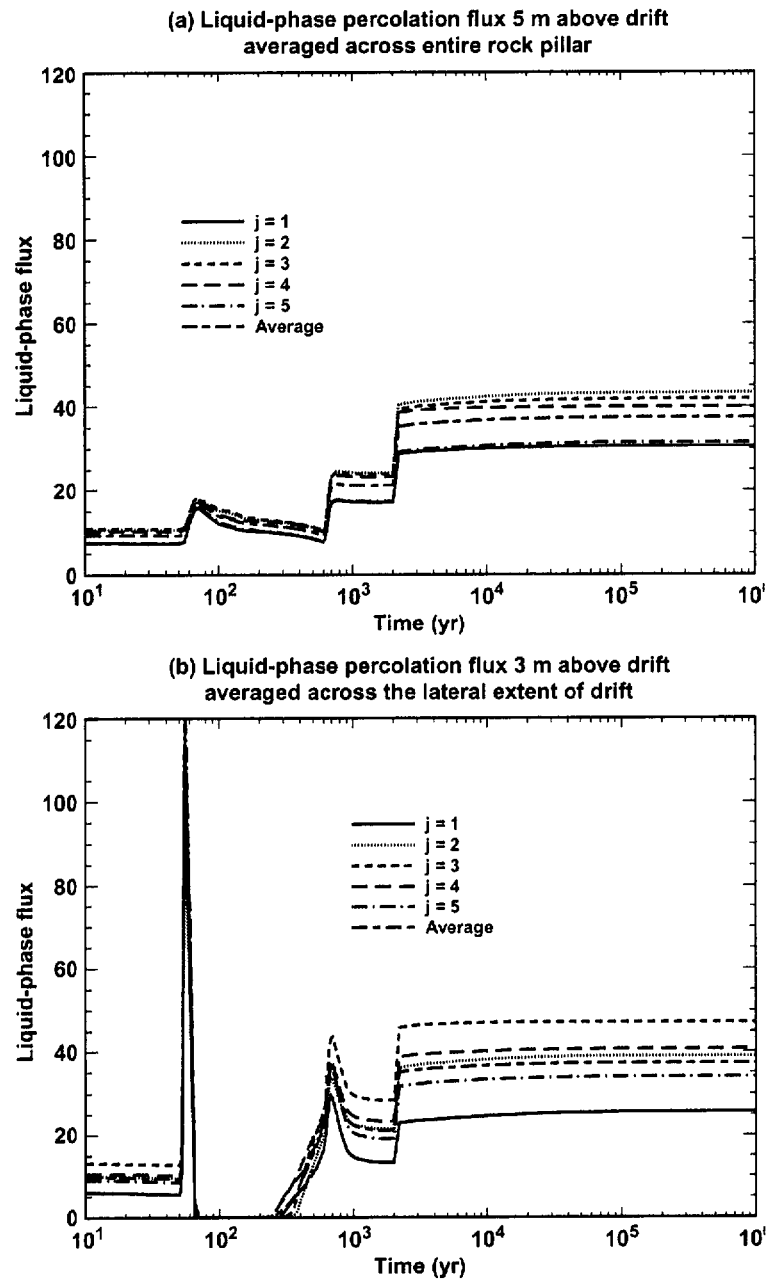
154_0198.ai

Source: Bodvarsson 2001 [DIRS 154669], Attachment 17, pp. 72 and 73.

NOTE: Fracture liquid fluxes (a) at a horizontal plane 5 m above the drift crown, and (b) at a horizontal plane along the drift center. Test conditions: heat load of 1.35 kW/m, ventilation of 80 percent removal over 300 years, and base case infiltration of 4.7879 mm/yr.

Figure 4.3.5-8. Fracture Liquid Fluxes as a Function of Lateral Distance from Drift Center for the Lower-Temperature Case

C18



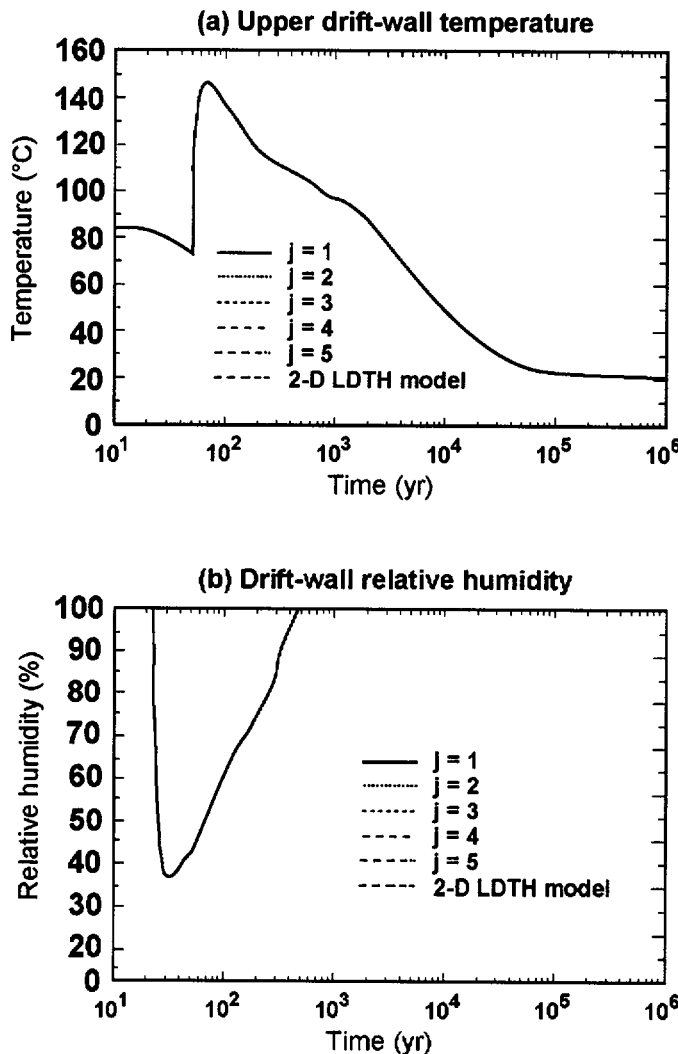
154_0199.ai

154_0199.ai

Source: BSC 2001 [DIRS 154985], Figure 6-96.

NOTE: Stochastic Realization C-56 and an areal mass loading of 56 MTU/acre. This realization assumes a \log_{10} standard deviation of 1.0, which is reasonably close to the measured value of 0.72 in Niche 2 (Station 36 + 50). Histories are given at five longitudinal locations ($j = 1, 2, 3, 4$, and 5) and for the equivalent two-dimensional homogeneous line-averaged-heat-source, drift-scale, thermal-hydrologic model. All liquid-phase fluxes at the drift wall and in the drift are zero for this case. Test conditions for (a): liquid-phase percolation flux 5 m above drift, averaged across the entire rock pillar. Test conditions for (b): liquid-phase percolation flux 3 m above drift, averaged across the lateral extent of the drift. Liquid-phase flux in mm/yr.

Figure 4.3.5-9. Liquid-Phase-Flux Histories at Various Locations in the Host Rock



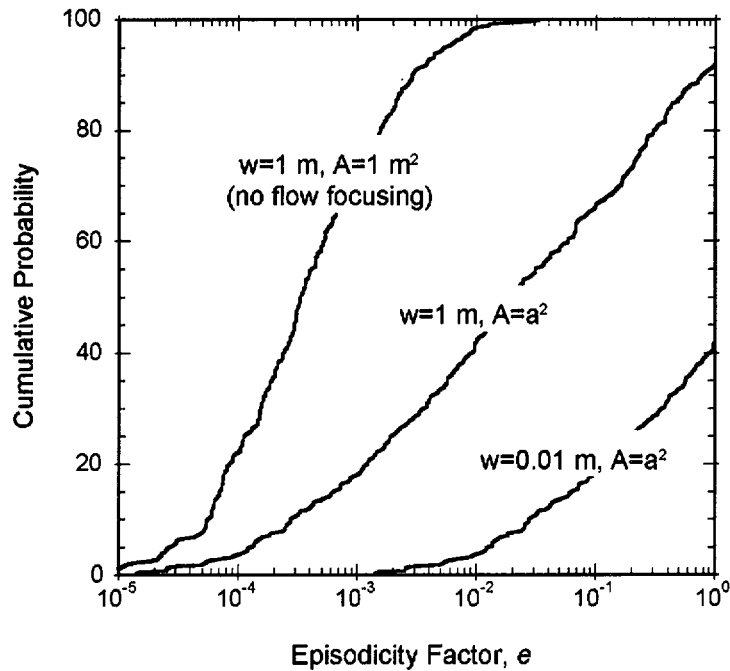
154_0200.ai

154_0200.ai

Source: BSC 2001 [DIRS 154985], Figure 6-95.

NOTE: Stochastic Realization C-56 and an areal mass loading of 56 MTU/acre (a) for upper drift wall temperature and (b) for drift wall relative humidity. This realization assumes a \log_{10} standard deviation of 1.0, which is reasonably close to the measured value of 0.72 in Niche 2 (Station 36 + 50). Histories are given at five longitudinal locations ($j = 1, 2, 3, 4$, and 5) and for the equivalent two-dimensional homogeneous line-averaged-heat-source, drift-scale, thermal-hydrologic model. The curves for all five locations and the two-dimensional model coincide. The local temperatures and relative humidities in the host rock are insensitive to drift-scale heterogeneity of permeability.

Figure 4.3.5-10. Temperature and Relative Humidity History at the Drift Wall



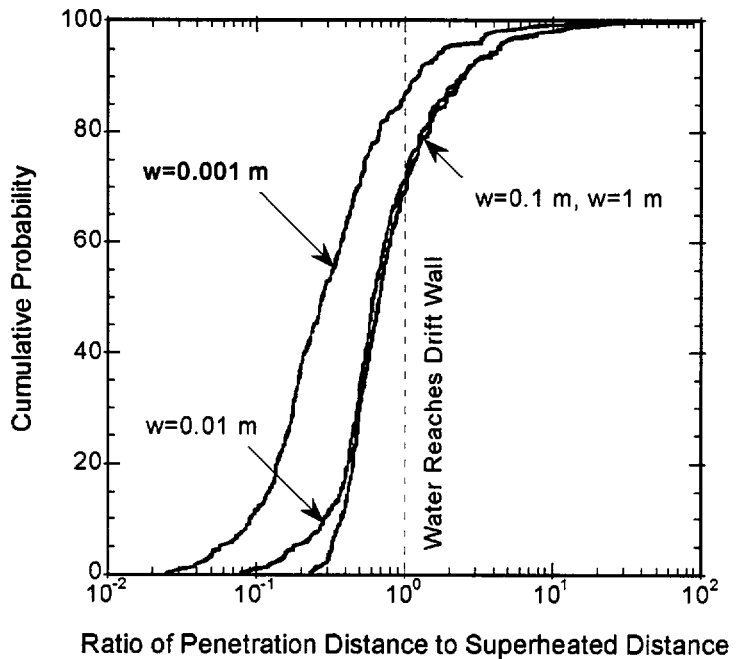
154_0201.ai

154_0201.ai

Source: DTN: SN0104T0511599.004 [DIRS 154713]

NOTE: $A = a^2$ indicates flow focusing; $A = 1 \text{ m}^2$ indicates no focusing.

Figure 4.3.5-11. Cumulative Distribution Function of the Episodicity Factor for Different Weep Widths and Flow Focusing Conditions



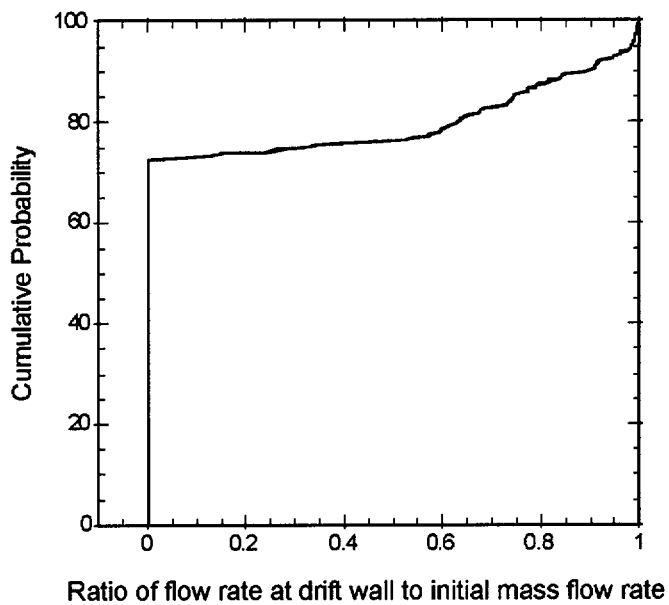
154_0202.ai

154_0202.ai

Source: DTN: SN0104T0511599.004 [DIRS 154713]

NOTE: Cumulative probability functions for the ratio of the penetration distance to superheated distance for infiltrating water using the three-dimensional solution in Phillips 1996 [DIRS 152005]; w = weep width.

Figure 4.3.5-12. Cumulative Probability for the Ratio of Penetration Distance to Superheated Distance



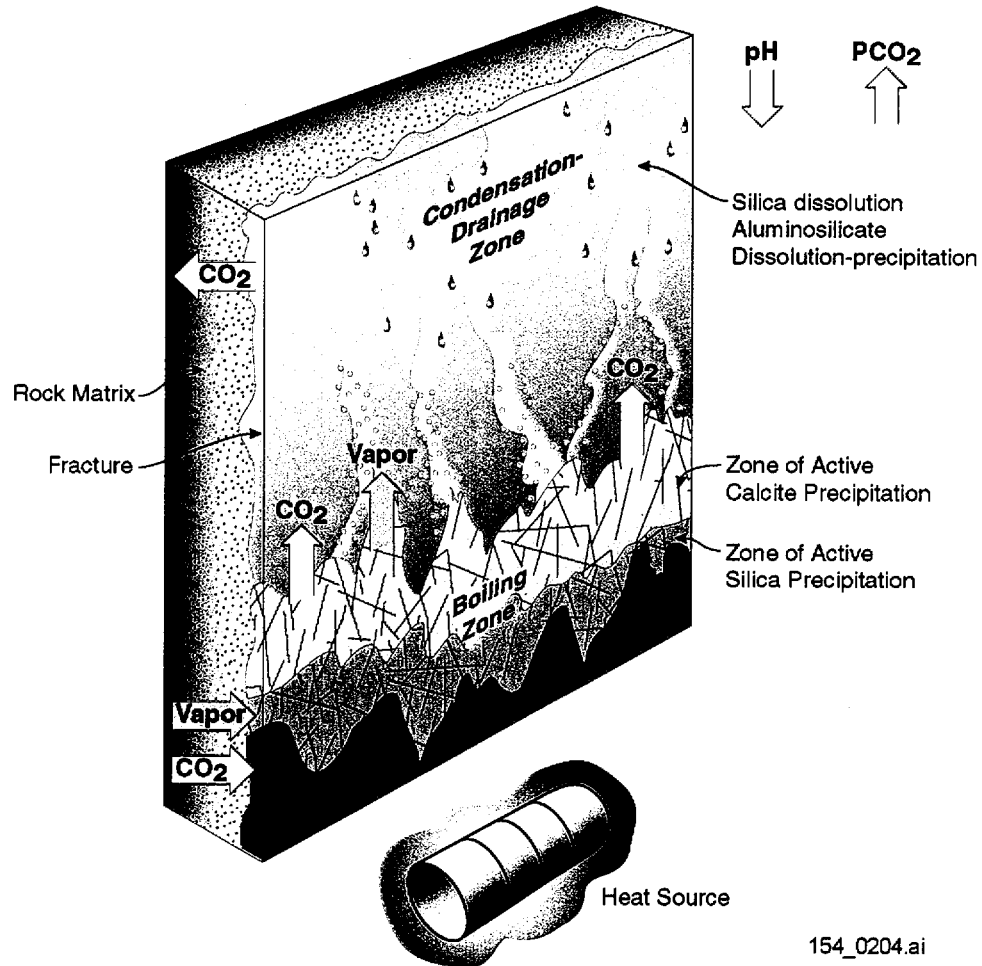
154_0203.ai

154_0203.ai

Source: DTN: SN0104T0511599.004 [DIRS 154713]

NOTE: Weep width = 1 m.

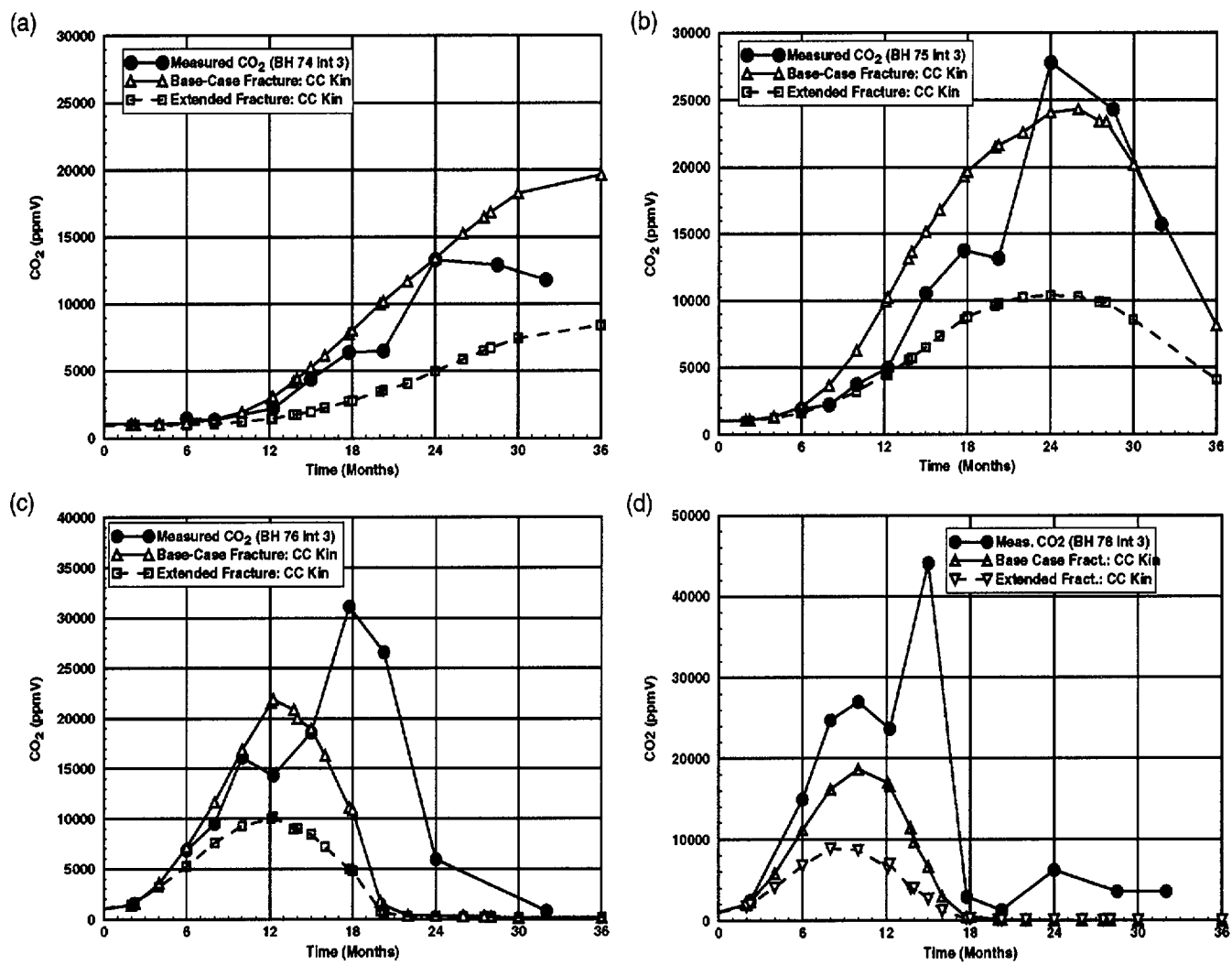
Figure 4.3.5-13. Cumulative Probability of the Ratio of the Mass Flow Rate at the Drift Wall to the Initial Mass Flow Rate



154_0204.ai

154_0204.ai

Figure 4.3.6-1. Schematic Diagram of the Relation between Thermal-Hydrologic Processes and Geochemical Processes



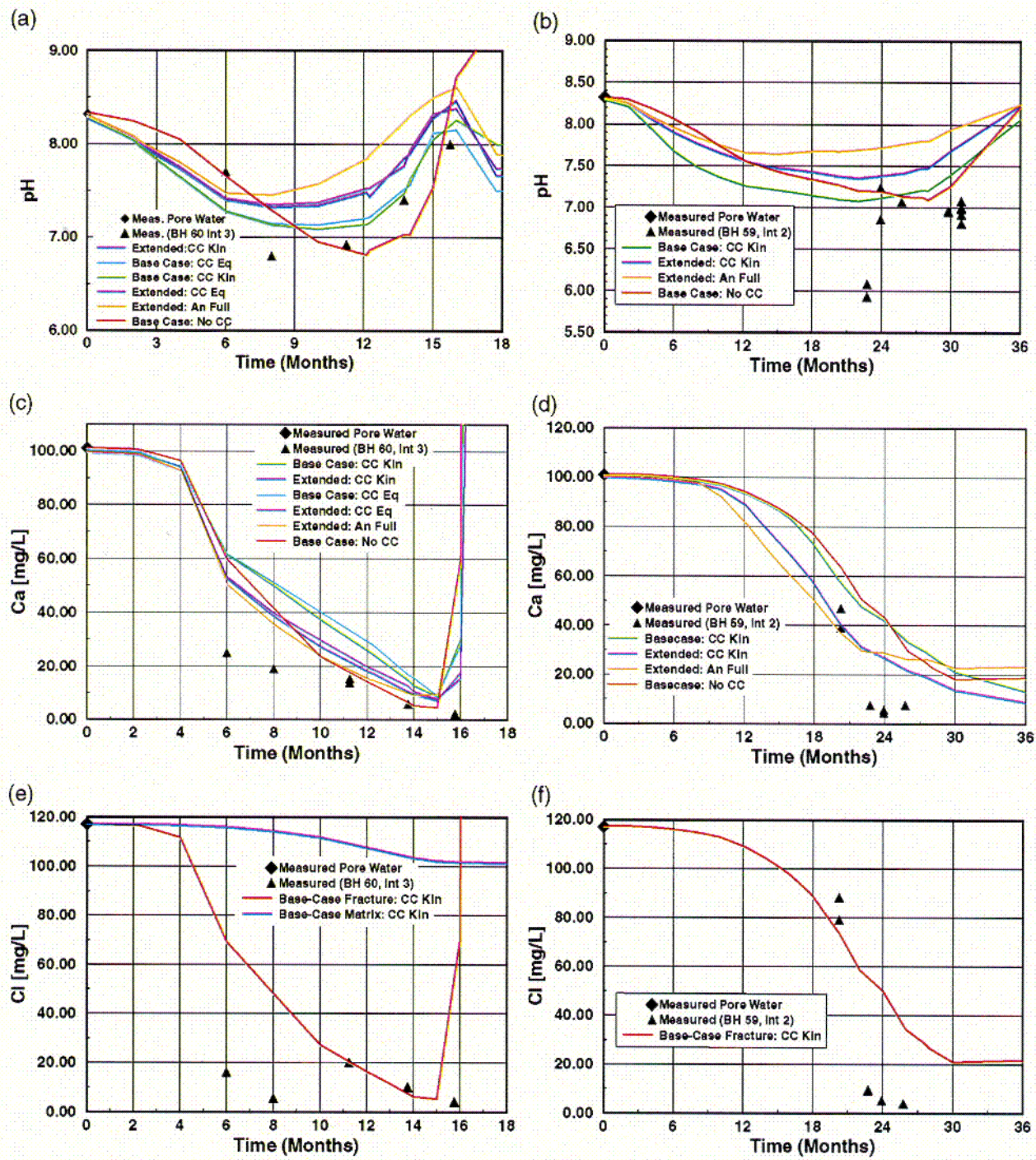
154_0205.ai

Source: BSC 2001 [DIRS 154667], Figure 18.

NOTE: CO₂ = gas-phase carbon dioxide, BH = borehole. Base case CC kin and extended-case CC kin in fractures to measured concentrations in boreholes: (a) borehole interval 74-3 at node above interval; (b) borehole interval 75-3; (c) borehole interval 76-3; (d) borehole interval 78-3 at node near end of interval.

154_0205.ai

Figure 4.3.6-2. Comparison of Modeled Carbon Dioxide Concentrations



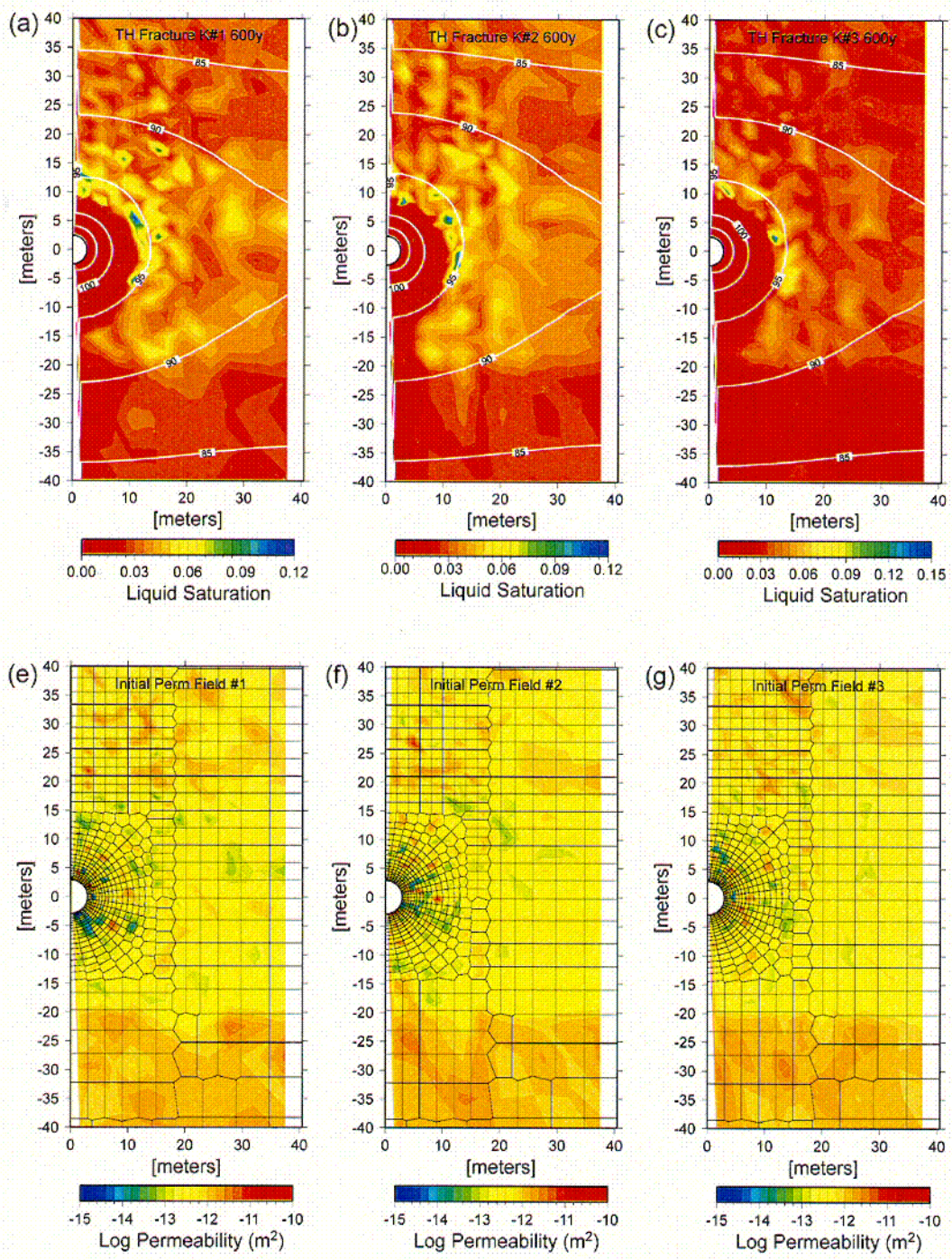
154_0206.ai

Source: BSC 2001 [DIRS 154667], Figures 19 (pH), 20 (chloride), and 23 (calcium).

NOTE: Changes in pH, total calcium, and total chloride in water samples collected from borehole intervals 60-3 and 59-2 compared to modeled fracture water compositions at nearby model grid nodes. The ambient pore water composition of each component is shown as a diamond at time zero on each plot.

Figure 4.3.6-3. Measured and Modeled Fracture Water Compositions

c19



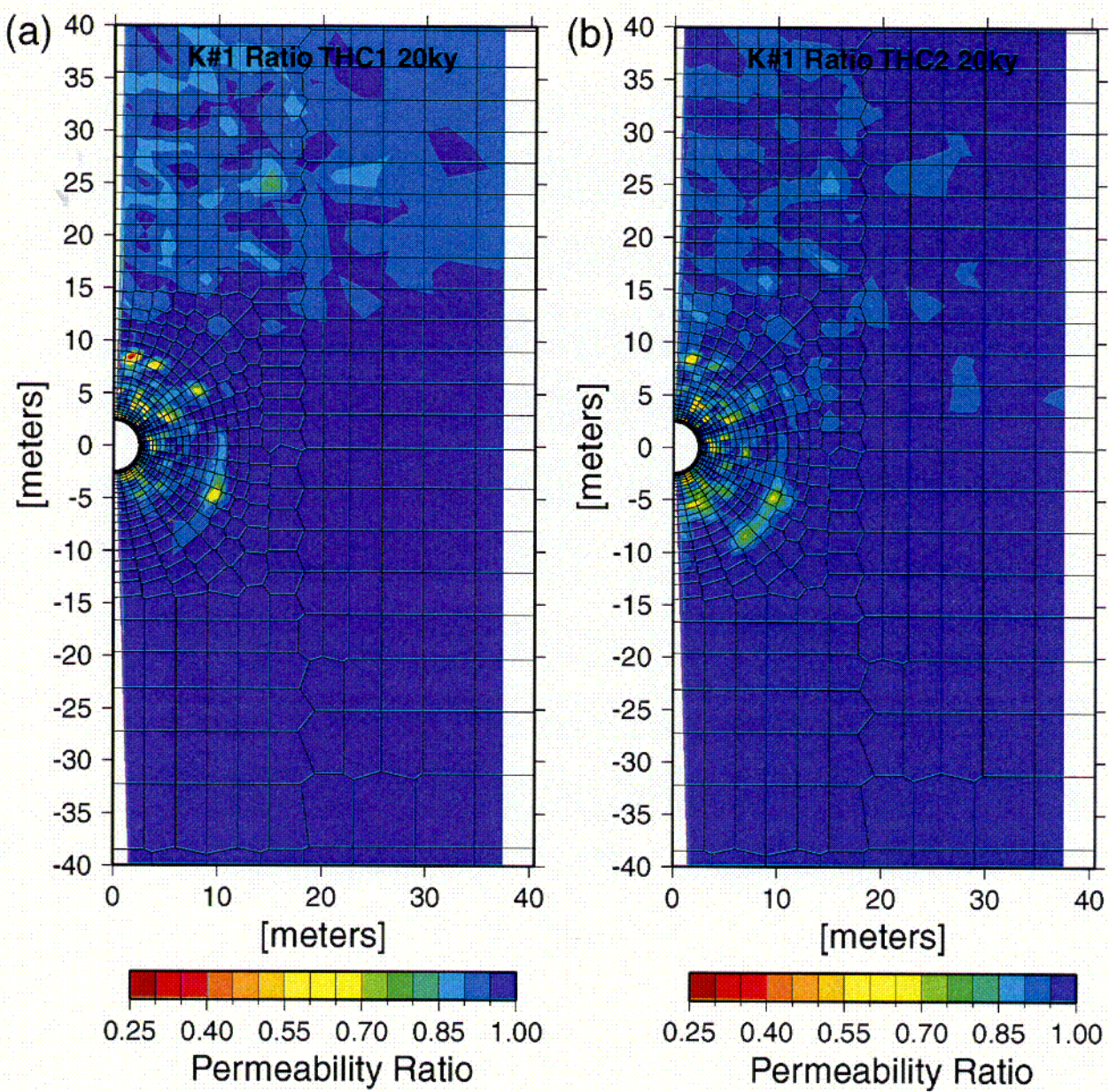
154_206a.eps

Source: BSC 2001 [DIRS 154667], Figure 74.

NOTE: Infiltration rate = 6 mm/yr; 600y = 600 Years; TH = thermal-hydrologic; k = permeability. Thermal-hydrologic simulations for (a) permeability realization #1, (b) realization #2, and (c) realization #3, (e) initial permeability realization #1, (f) initial permeability realization #2, (g) initial permeability realization #3. Model domain extends for a few hundred meters above and below area shown.

Figure 4.3.6-4. Fracture Liquid Saturations at 600 Years from Thermal-Hydrological Simulations for Three Permeability Realizations

C20



154_0209.ai

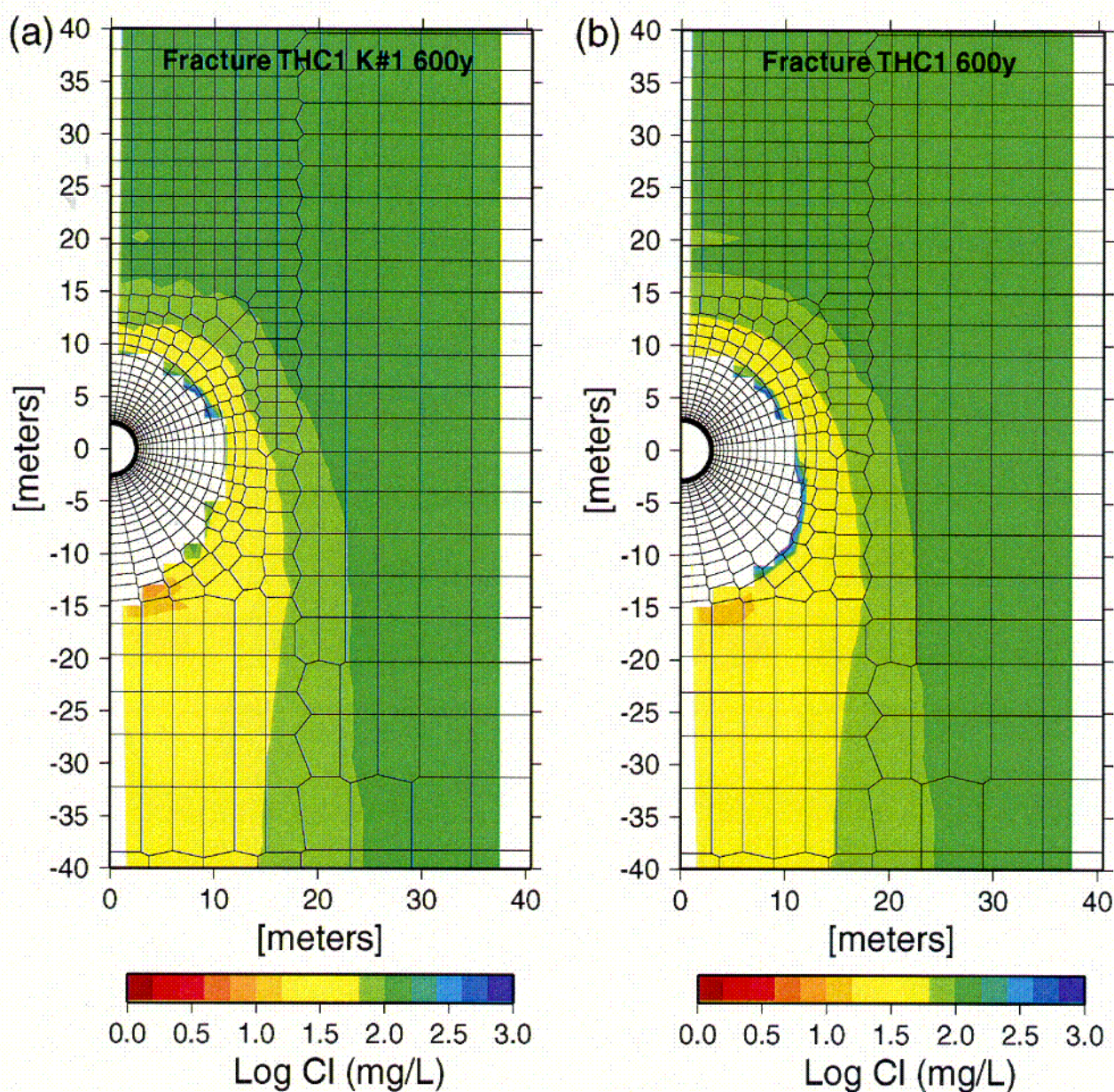
154_0209.ai

Source: BSC 2001 [DIRS 154667], Figure 75.

NOTE: 20ky = 20,000 years; THC = thermal-hydrologic-chemical; K = permeability. Results for (a) extended geochemical system, (b) base-case geochemical system. Model domain extends for a few hundred meters above and below area shown.

Figure 4.3.6-5. Fracture Permeability Ratio After 20,000 Years for Realization #1

C21



154_0211.ai

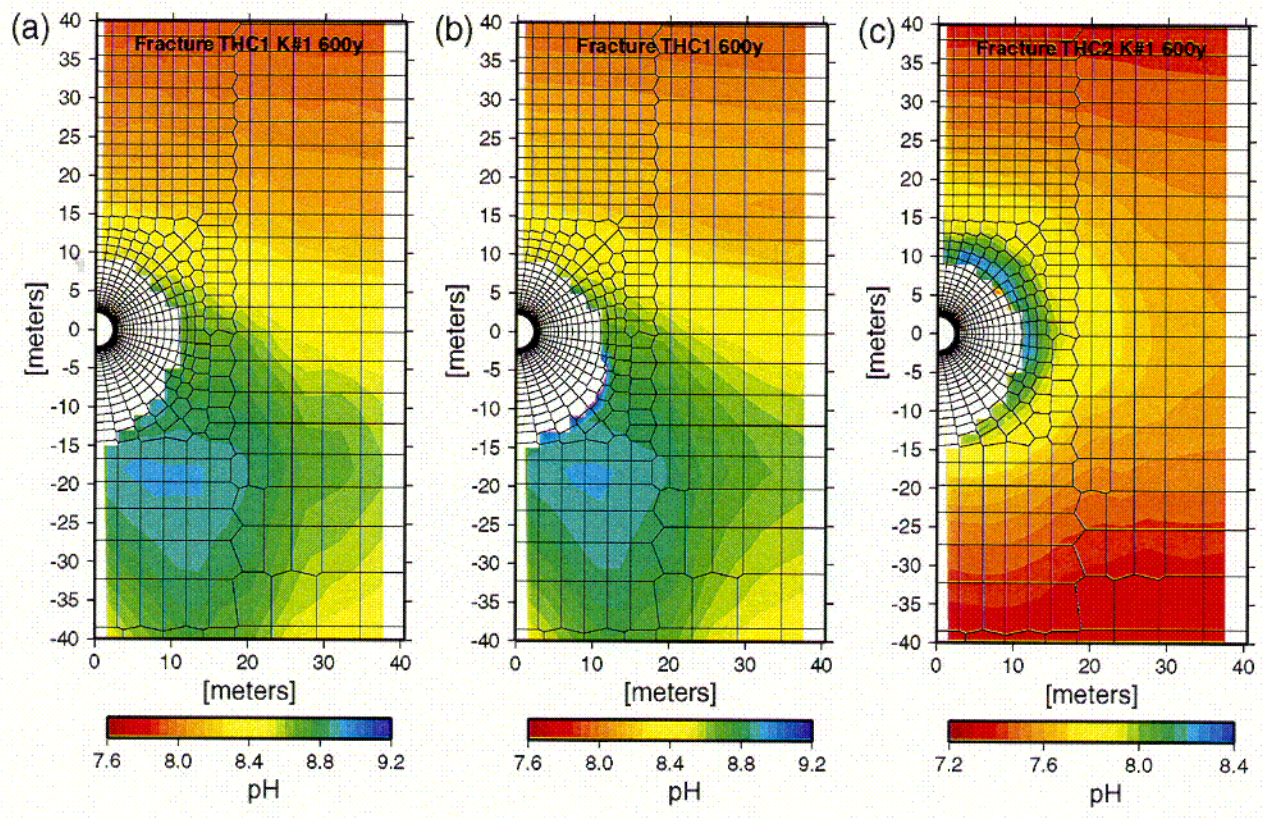
154_0211.ai

Source: BSC 2001 [DIRS 154667], Figure 82.

NOTE: THC = thermal-hydrologic-chemical; K = permeability; 600y = 600 Years. Results for (a) the extended geochemical system, permeability realization #1; (b) the extended geochemical system, initially homogeneous Tptpmn. Model domain extends a few hundred meters above and below area shown.

Figure 4.3.6-6. Chloride Concentrations in Fracture Water After 600 Years

222



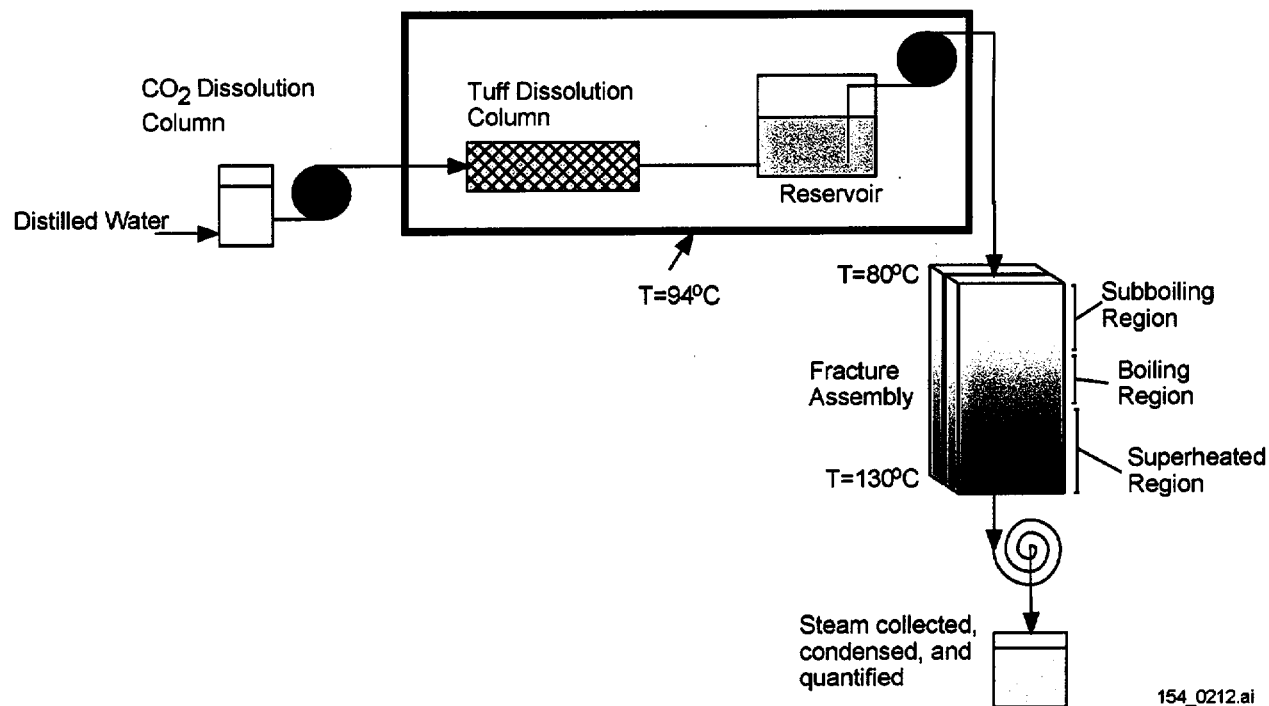
154_0210.ai

Source: BSC 2001 [DIRS 154667], Figure 80.

NOTE: THC = thermal-hydrologic-chemical; K = permeability; 600y = 600 Years. White area is dry. Results for (a) extended geochemical system, permeability realization #1; (b) extended geochemical system, initially homogeneous Tptpmn; (c) base-case geochemical system (heterogeneous permeability realization #1). Model domain extends a few hundred meters above and below area shown.

Figure 4.3.6-7. Fracture Water pH After 600 Years

C23

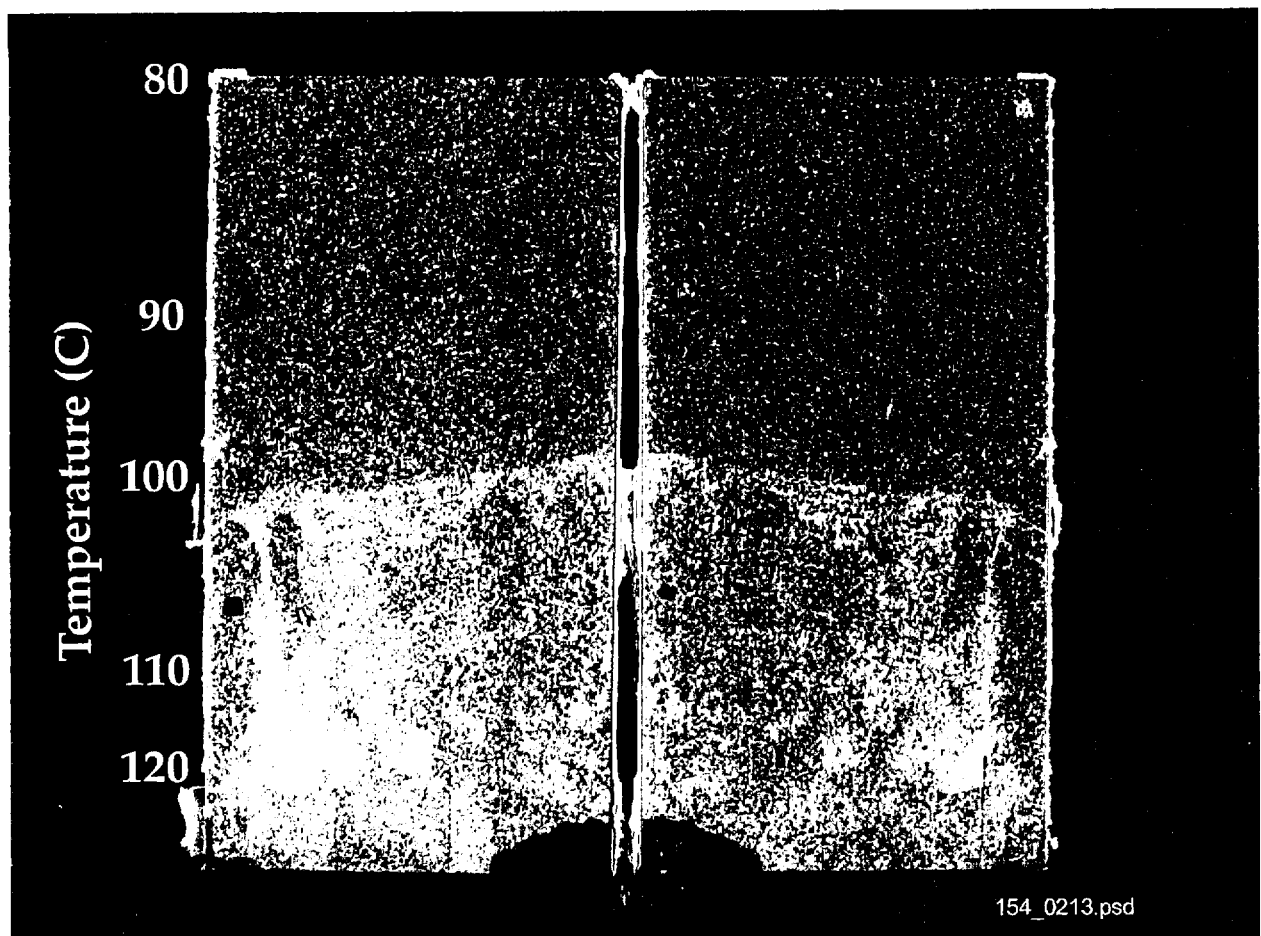


154_0212.ai

Source: Kneafsey et al. 2001 [DIRS 154460], Figure 1.

NOTE: CO₂ = carbon dioxide, T = temperature.

Figure 4.3.6-8. Schematic of Experiment to Replicate Mineral Dissolution and Precipitation by Condensate-Water in Fractured Tuff

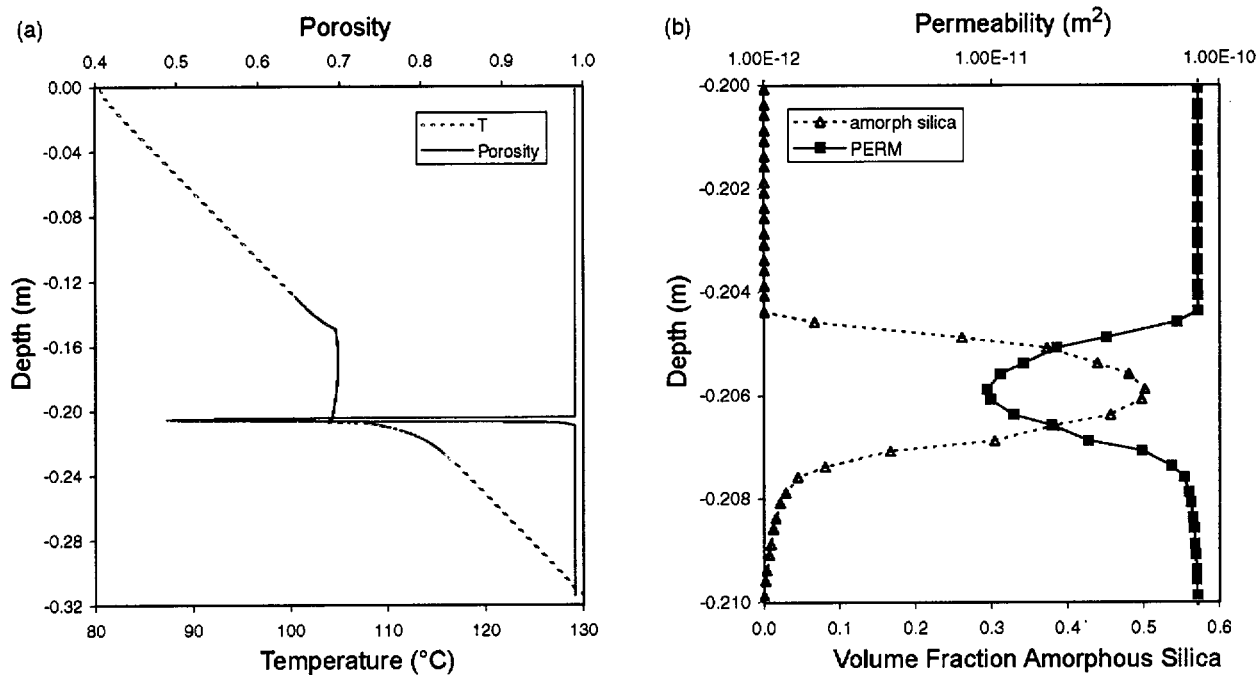


154_0213.psd

Source: Kneafsey et al. 2001 [DIRS 154460], Figure 2.

NOTE: Enhanced image showing fracture temperature profile and fluorescing precipitate (light shades) under ultraviolet illumination on both fracture faces. Vertical fracture dimension is 0.317 m.

Figure 4.3.6-9. Image of a Fracture Opened at the Conclusion of an Experiment to Examine Precipitate Location, Mineralogy, and Morphology



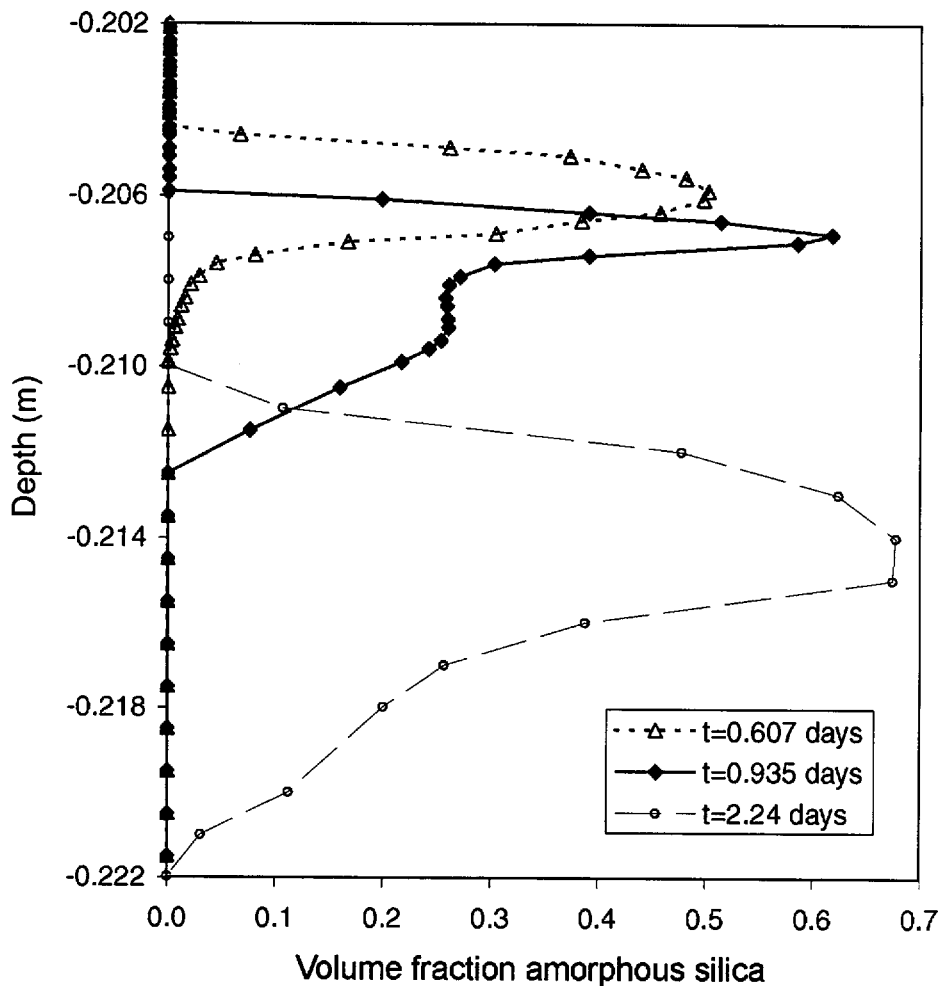
154_0214.ai

154_0214.ai

Source: Bodvarsson 2001 [DIRS 154669], Attachment 4, p. 35.

NOTE: T = time; amorph = amorphous; PERM = permeability. Depth profiles for (a) temperature and porosity, and (b) permeability and amorphous silica precipitation for a simulated fracture plugging experiment at 0.6 days. Depth interval for (b) is located at the base of the two-phase zone. The porosity and permeability reduction, caused by amorphous silica precipitation, occurs at the base of the boiling front.

Figure 4.3.6-10. Depth Profiles for a Simulated Fracture Plugging Experiment



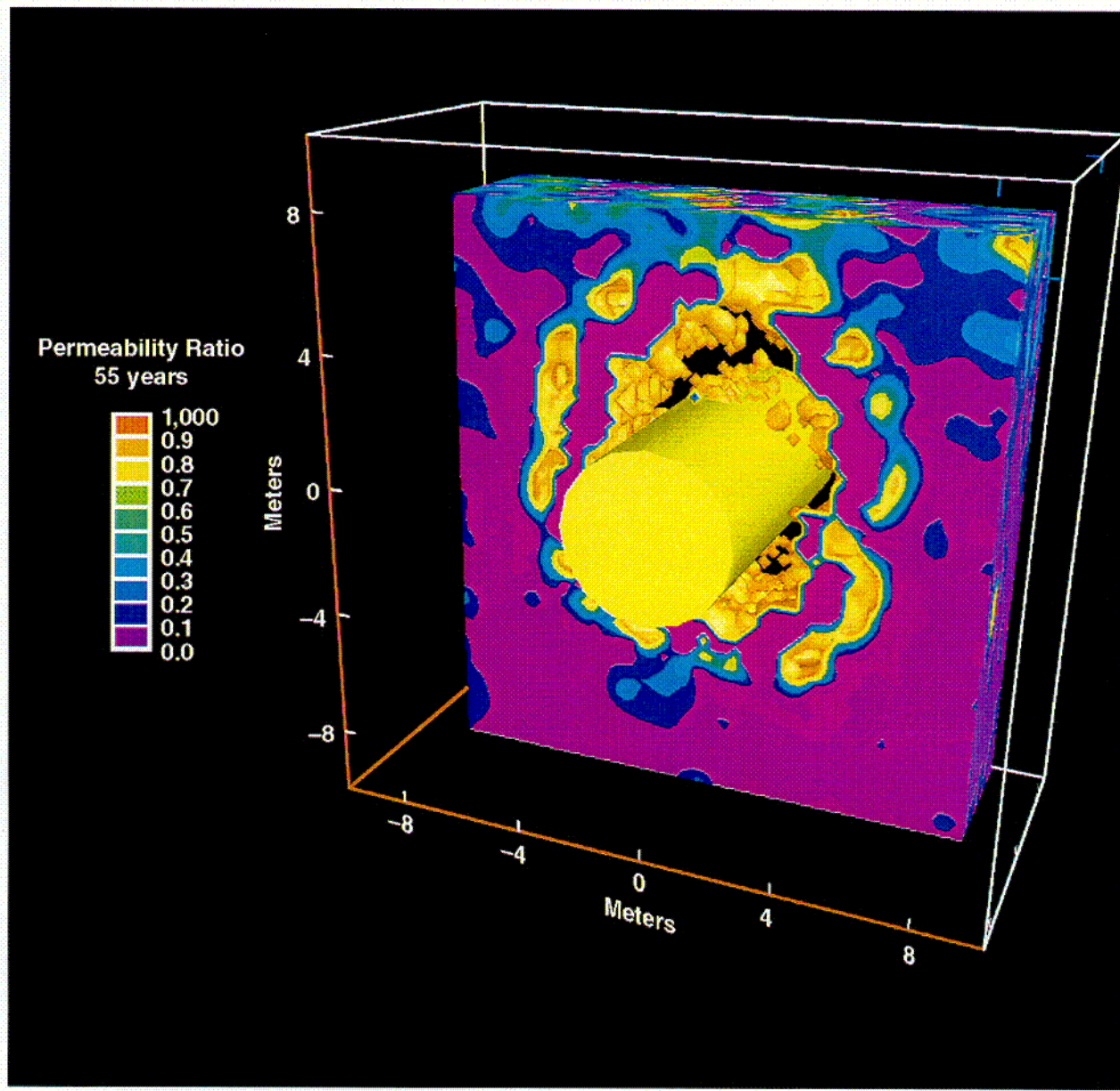
154_0215.ai

154_0215.ai

Source: Bodvarsson 2001 [DIRS 154669], Attachment 4, p. 29.

NOTE: t = time. Volume fraction of precipitated amorphous silica at 0.6, 0.9, and 2.2 days. The upper portion of precipitated silica is redissolved over time as precipitation follows the boiling front downward. Maximum porosity reduction approaches 70% over the time span of the simulation.

Figure 4.3.6-11. Precipitated Amorphous Silica for Simulated Fracture Plugging Experiment



154_0478.ai

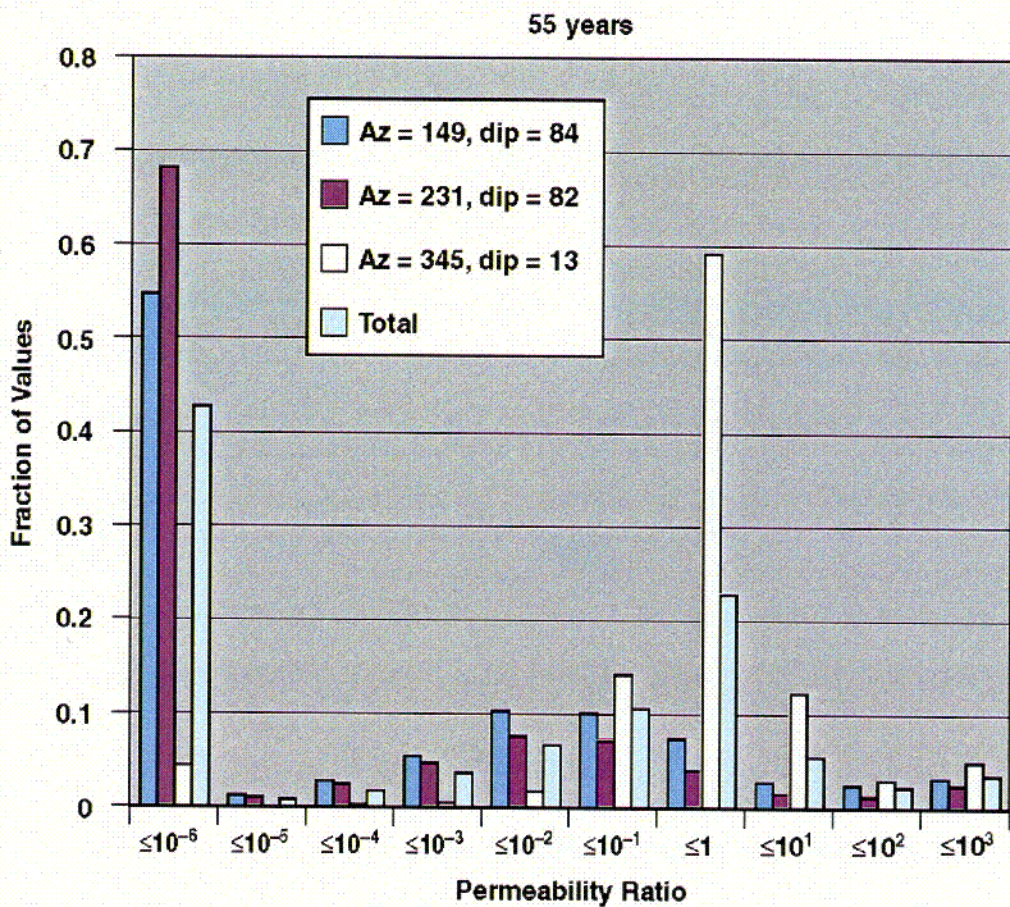
154_0478.ai

Source: Blair 2001 [DIRS 155005] p. 90.

NOTE: Zones of increased permeability removed.

Figure 4.3.7-1. Permeability Ratios at 55 Years for Higher-Temperature Case

C24



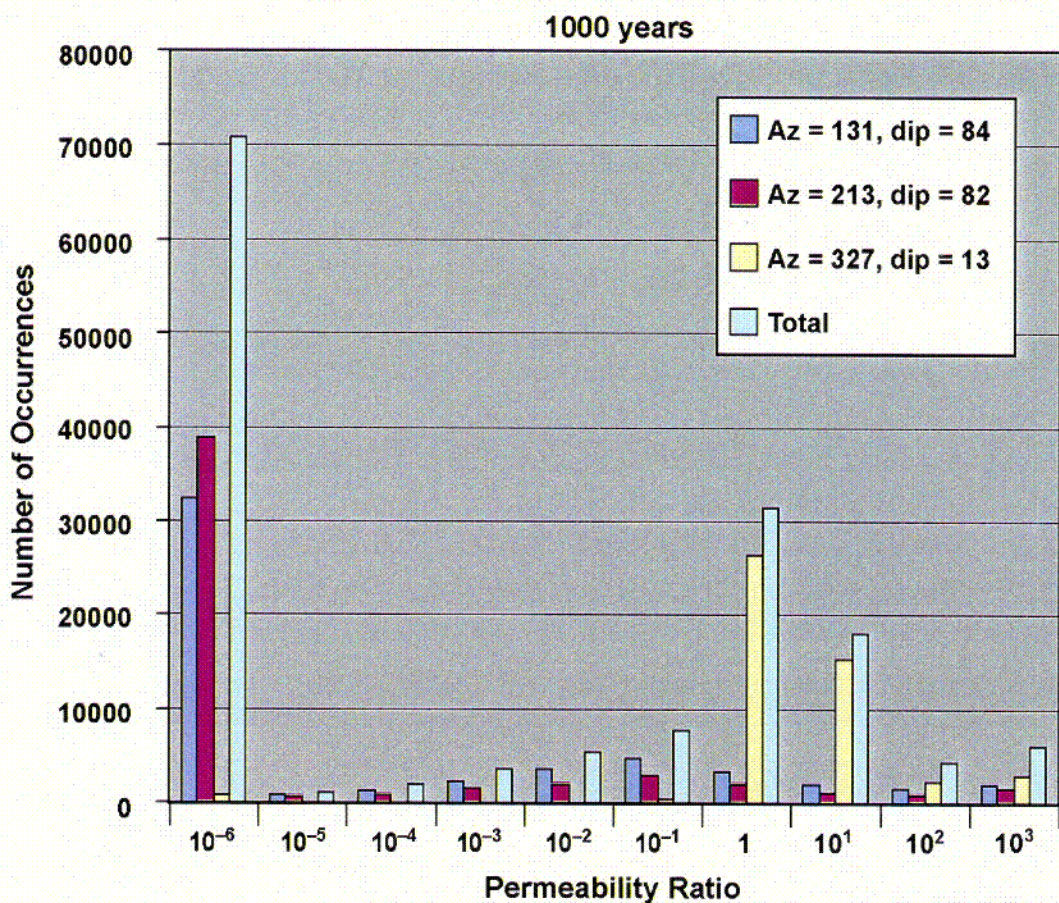
154_0479.ai

154_0479.ai

Source: Blair 2001 [DIRS 155005], p. 91.

NOTE: The histogram bins each span one order of magnitude, except for the lowest, which includes all permeability ratios below 10^{-6} .

Figure 4.3.7-2. Histogram of Permeability Ratios at 55 Years for Each Fracture Set for Higher-Temperature Case

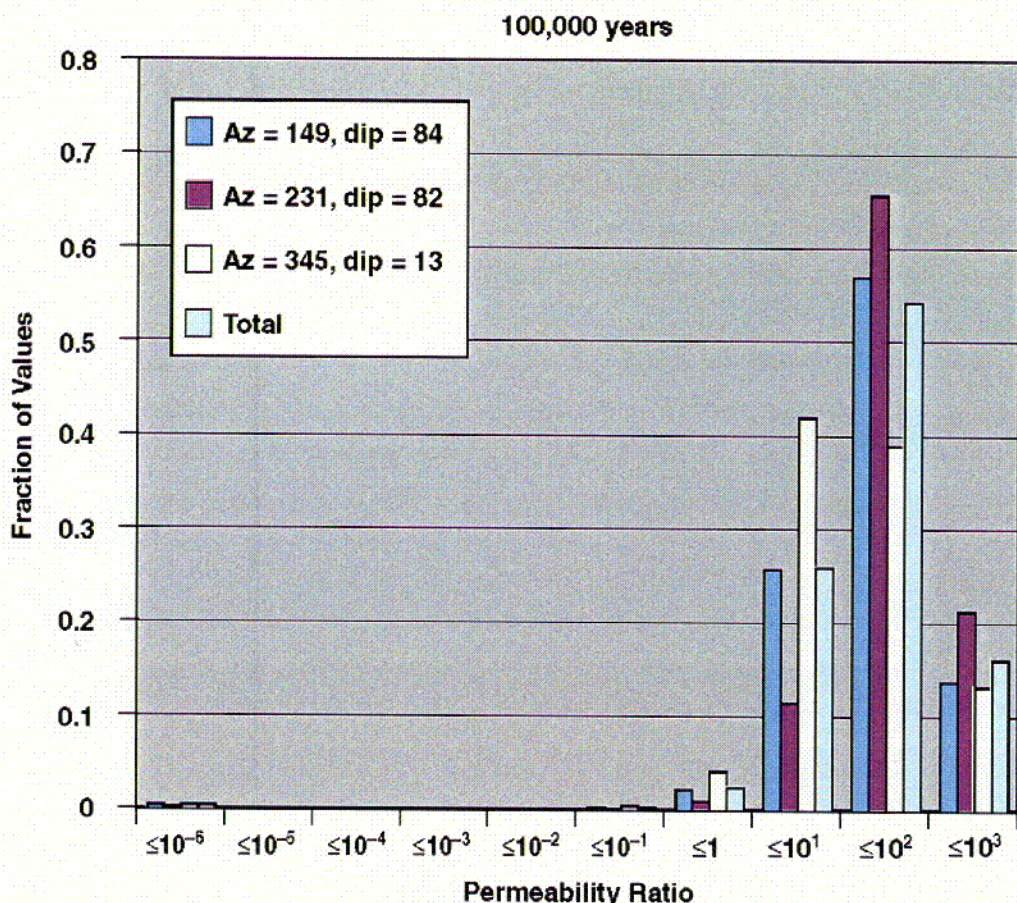


154_0480.ai

154_0480.ai

Source: Blair 2001 [DIRS 155005], p. 106.

Figure 4.3.7-3. Histograms of Permeability Ratios at 1,000 Years for Each Fracture Set for the Higher-Temperature Case



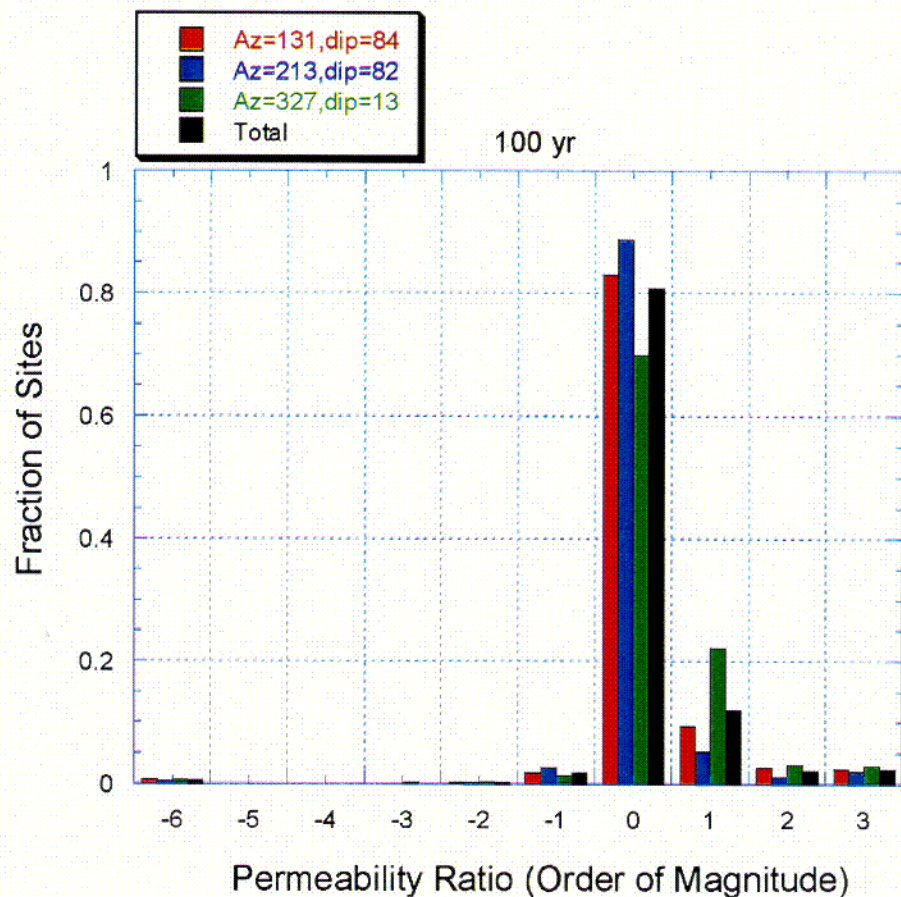
154_0481.ai

154_0481.ai

Source: Blair 2001 [DIRS 155005], p. 108.

NOTE: The histogram bins each span one order of magnitude, except for the lowest, which includes all permeability ratios below 10^{-6} .

Figure 4.3.7-4. Histogram of Permeability Ratios at 100,000 Years for Each Fracture Set for the Higher-Temperature Case



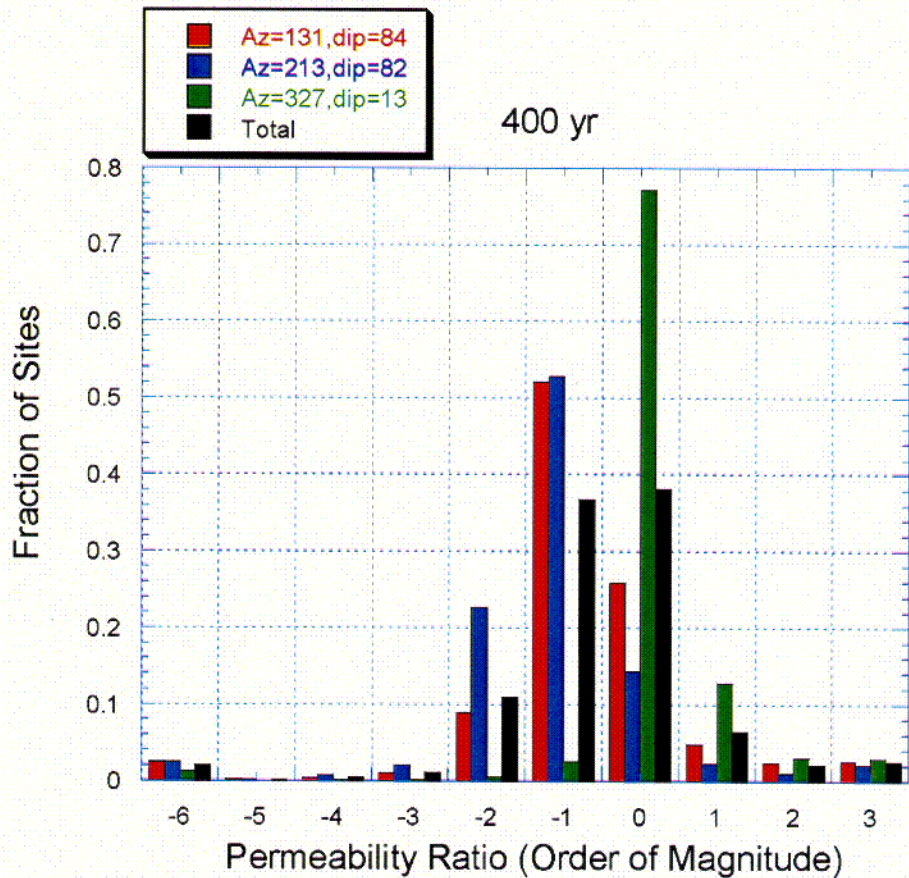
154_0526.ai

Source: Blair 2001 [DIRS 155005].

Figure 4.3.7-4a. Fracture Permeability Multipliers for the Lower-Temperature Operating Mode Case 100 Years after Emplacement

154_0526.ai

C28



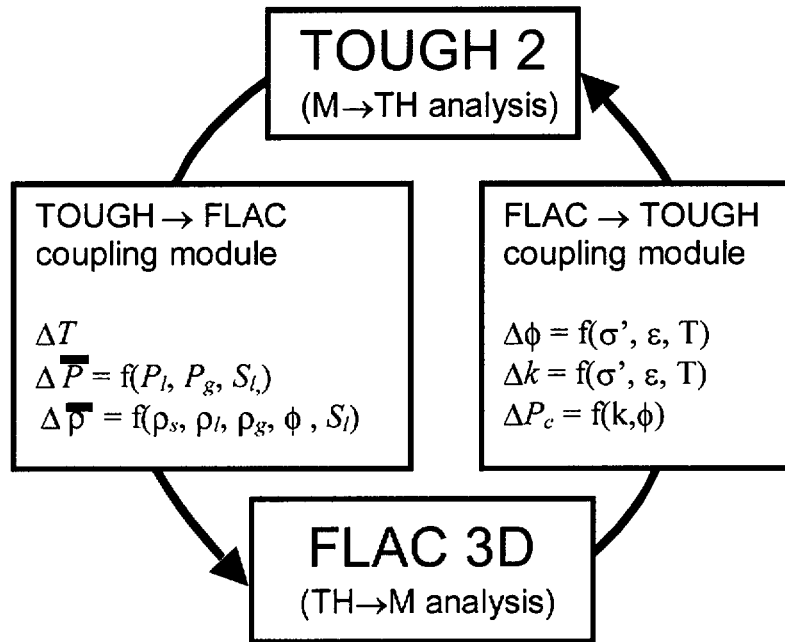
154_0527.ai

Source: Blair 2001 [DIRS 155005].

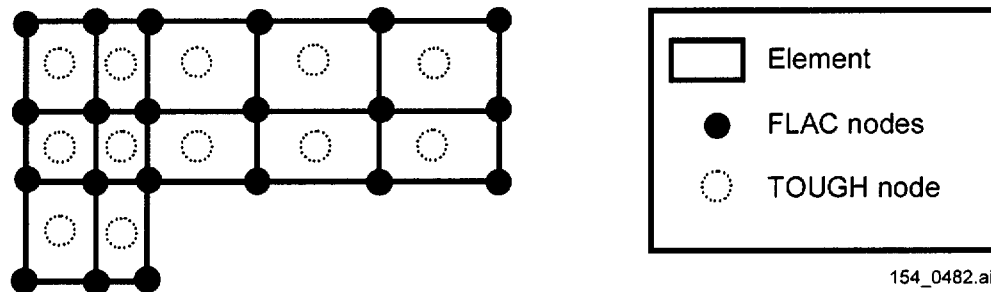
Figure 4.3.7-4b. Fracture Permeability Multipliers for the Lower-Temperature Operating Mode Case 400 Years after Emplacement

C29

(a)



(b)



154_0482.ai

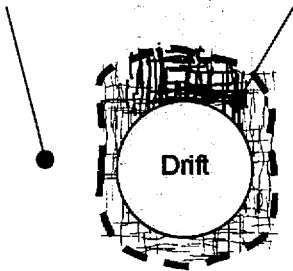
NOTE: TH = thermal-hydrologic, M = mechanical. Symbols: porosity (ϕ), permeability (k), effective stress (σ'), strain (ε), temperature (T), pressure (P), mean, solid, liquid, and gas densities respectively ($\bar{\rho}$, ρ_s , ρ_l , and ρ_g), liquid pressure (P_l), gas pressure (P_g), capillary pressure (P_c), liquid saturation (S_l).

Figure 4.3.7-5. Linking TOUGH2 and FLAC3D Codes

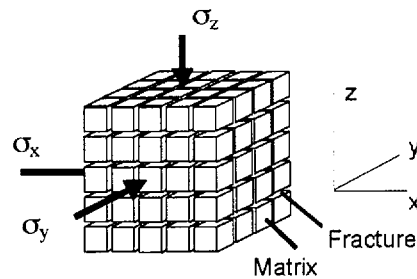
(a)

Away from drift: Basically linear or non-linear elastic mechanical response

Near drift opening: Significant inelastic mechanical response possible due to unloading against the free surface. The inelastic responses includes fracture slip and/or fracturing



(b)



$$k_x = k_x(\sigma_y, \sigma_z)$$

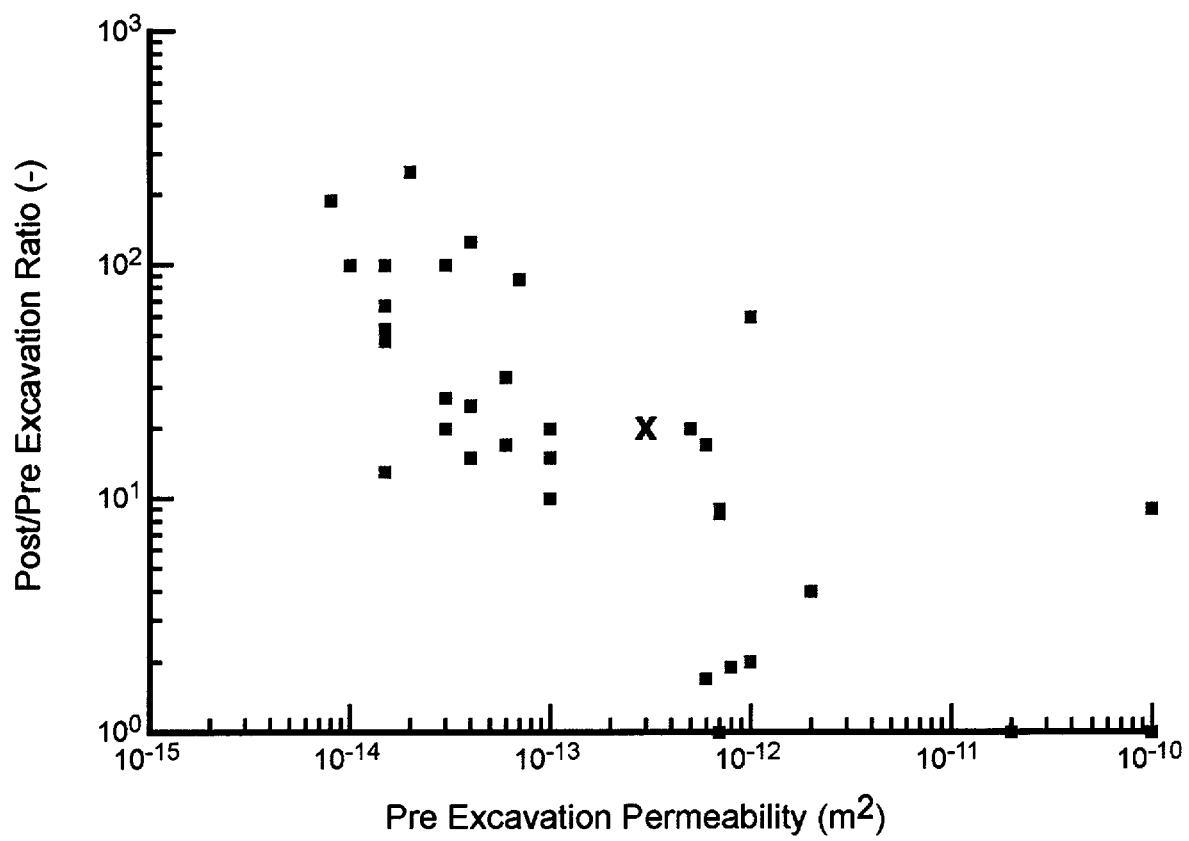
$$k_y = k_y(\sigma_x, \sigma_z)$$

$$k_z = k_z(\sigma_x, \sigma_y)$$

154_0483.ai

154_0483.ai

Figure 4.3.7-6. Schematic Diagram of the Fracture Rock System Near a Drift and the Conceptual Stress Permeability Model Used



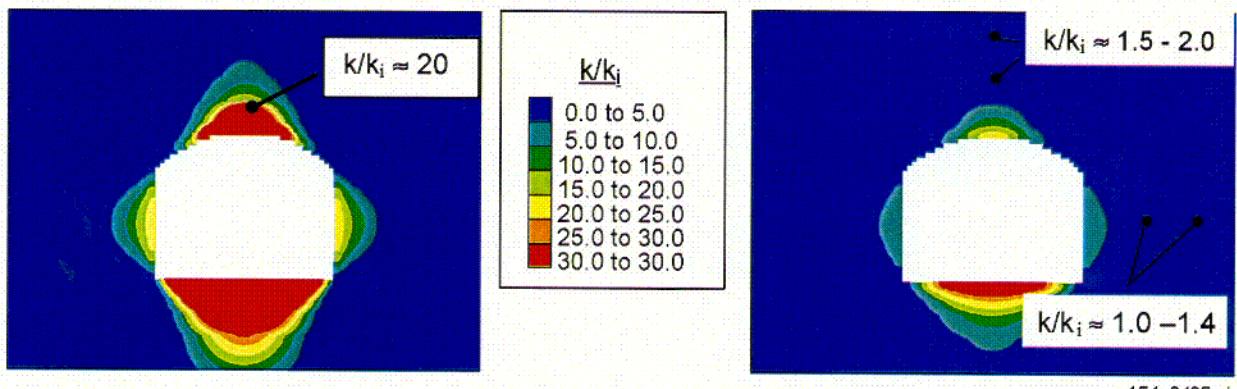
154_0484.ai

154_0484.ai

Source: Bodvarsson 2001 [DIRS 154669], Attachment 9, p.14.

NOTE: Data for Niche 2 (Station 36 + 50). The matching point for calibration is indicated by "x".

Figure 4.3.7-7. Changes in Post- to Pre-Excavation Permeability as a Function of Initial Permeability



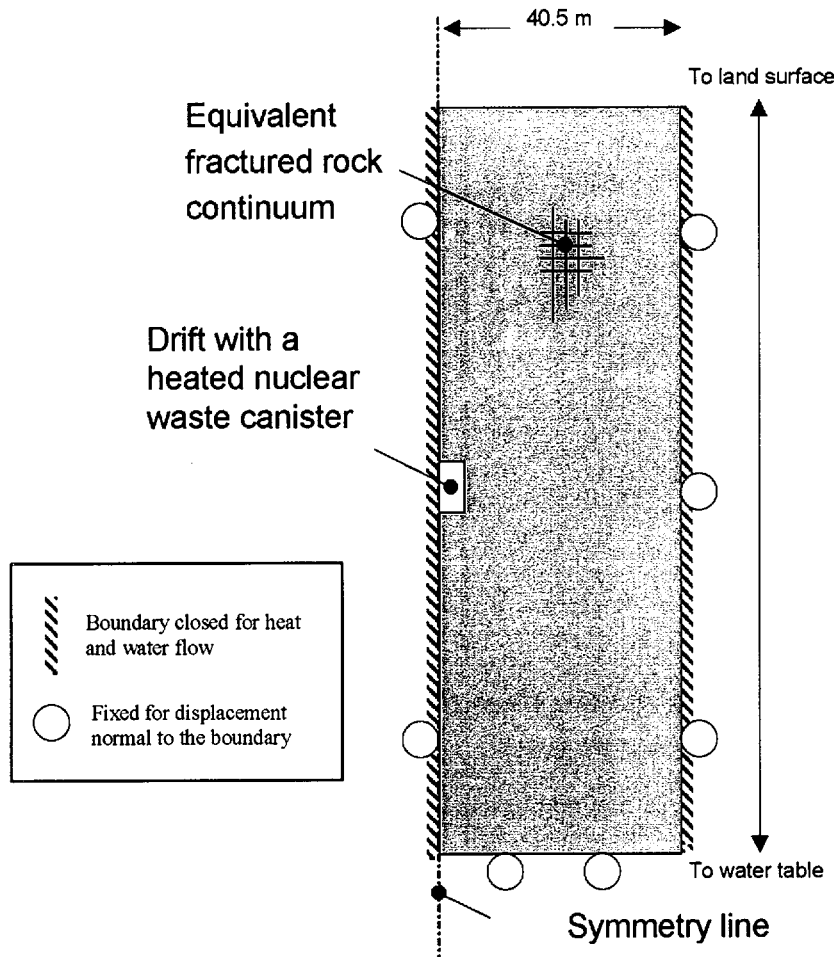
154_0485.ai

Source: Bodvarsson 2001 [DIRS 154669], Attachment 9, pp. 27 to 30.

NOTE: Data for niches in Tptpmn (left) and Tptpli (right).

Figure 4.3.7-8. Contour Plot of Pre- to Post-Excavation Permeability Ratio from the Calibrated Model

C30



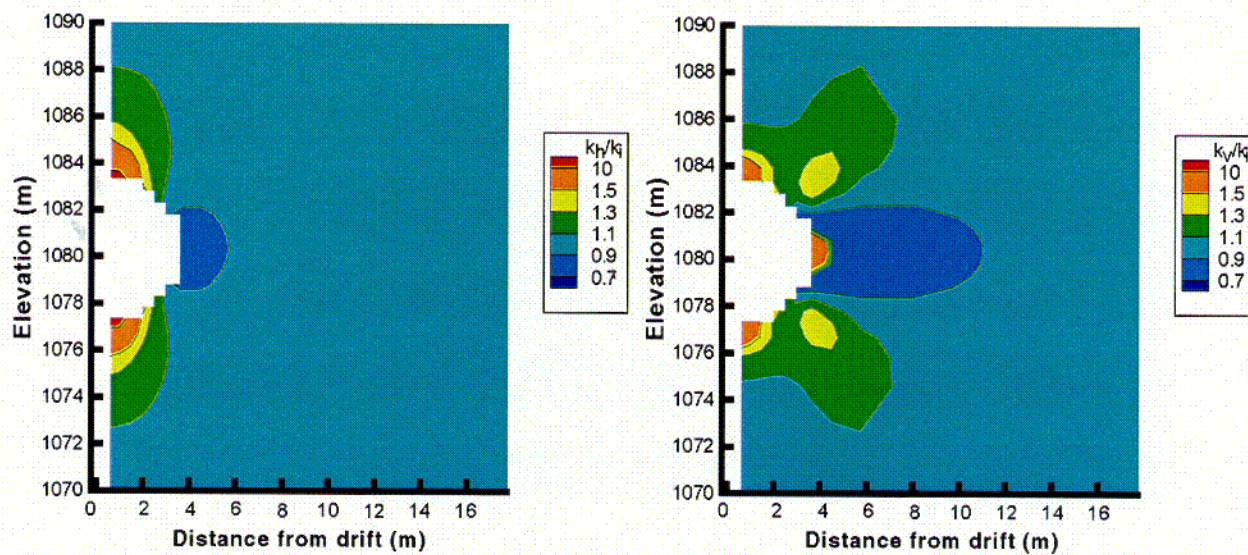
154_0486.ai

154_0486.ai

Source: Bodvarsson 2001 [DIRS 154669], Attachment 9, p. 34.

NOTE: Drift located in the Tptpl unit with 81-m drift spacing.

Figure 4.3.7-9. Model Geometry and Boundary Conditions for a Nuclear Waste Emplacement Drift



154_0487.ai

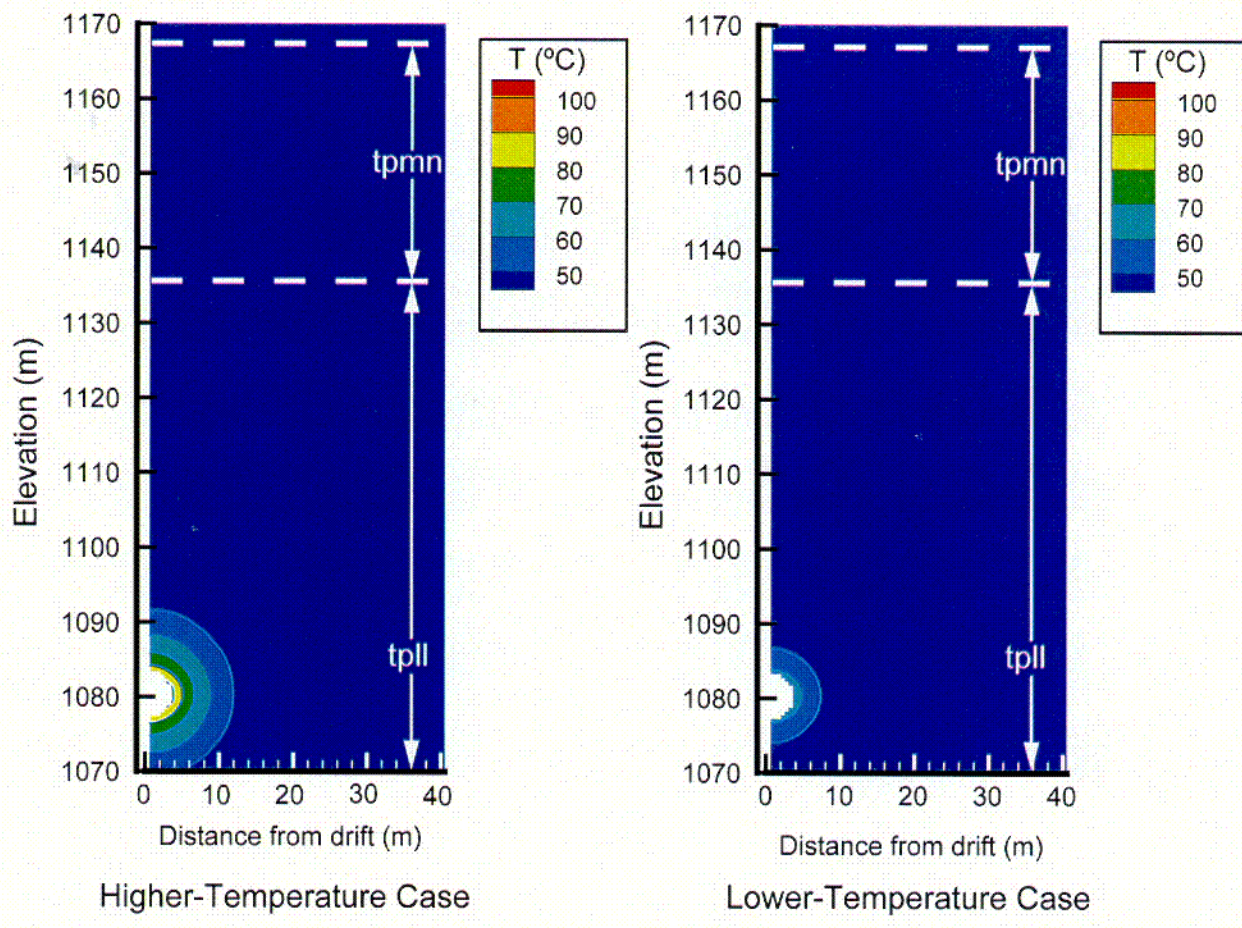
154_0487.ai

Source: Bodvarsson 2001 [DIRS 154669], Attachment 9, pp. 60 to 61.

NOTE: (a) horizontal, k_h , and (b) vertical, k_v , permeabilities.

Figure 4.3.7-10. Changes in Horizontal and Vertical Permeabilities Before and After Excavation

C31



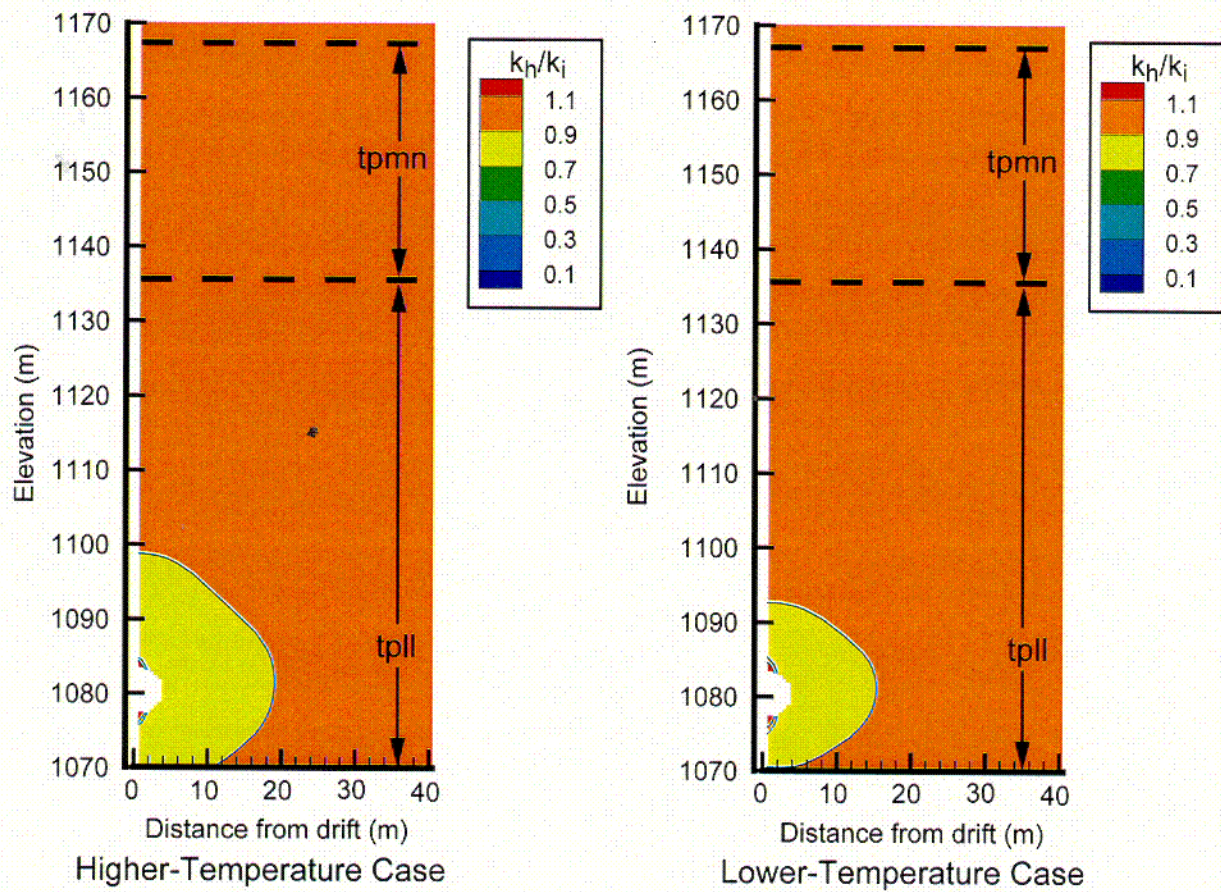
154_0488a.ai

Source: Bodvarsson 2001 [DIRS 154669], Attachment 9, p. 65.

Figure 4.3.7-11. Temperature Distribution at 10 Years

154_0488a.ai

C 32

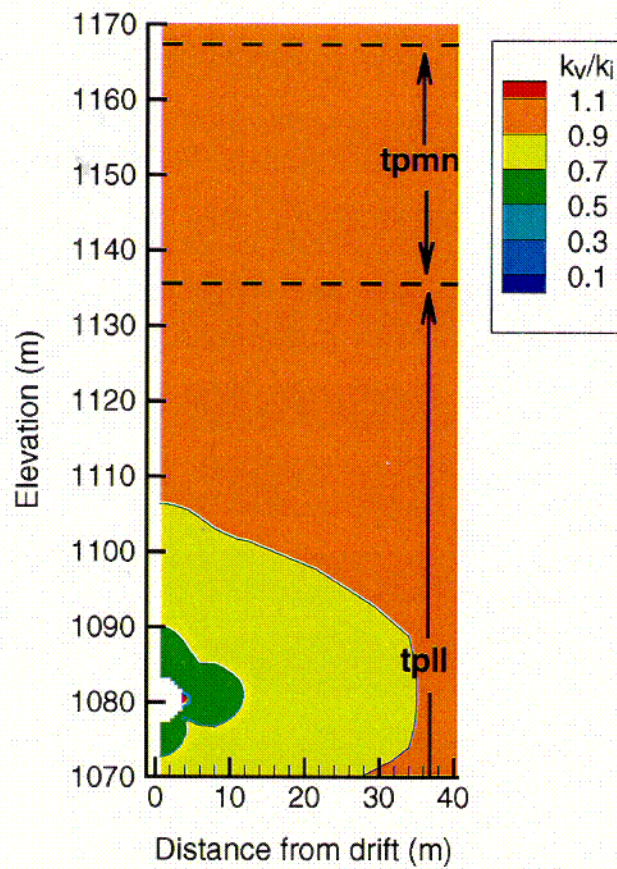


154_0489a.ai

Source: Bodvarsson 2001 [DIRS 154669], Attachment 9, pp. 57 to 74.

Figure 4.3.7-12. Horizontal Permeability Changes at 10 Years

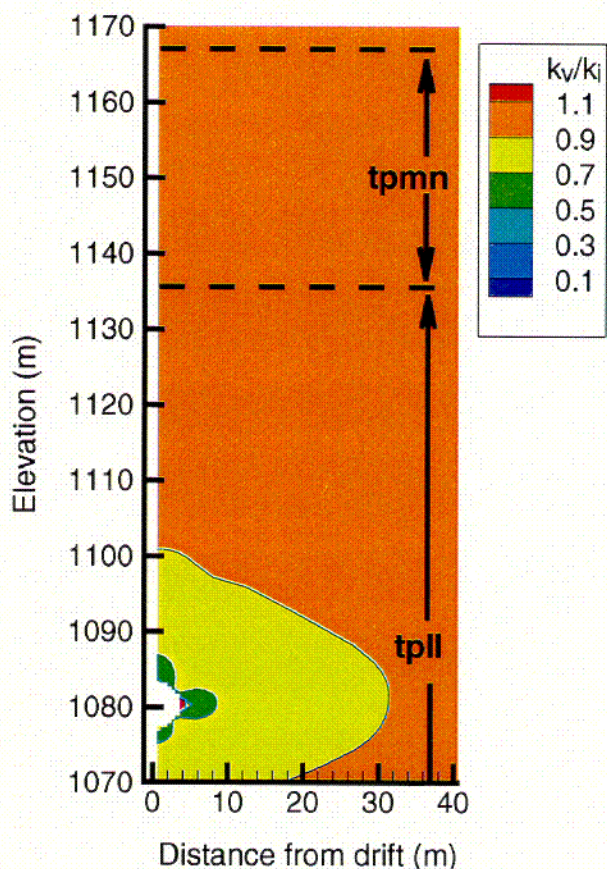
C33



Higher-Temperature Case

154_0490a.ai

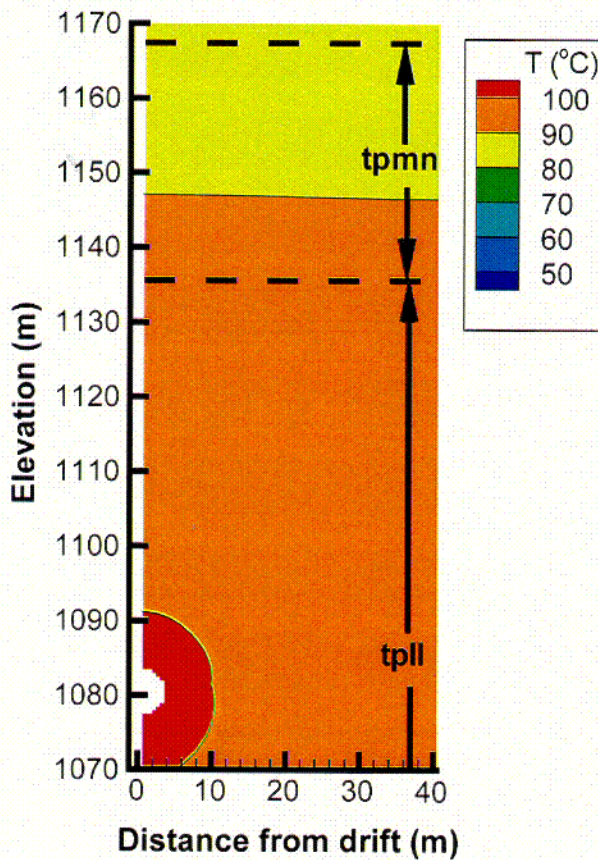
Source: Bodvarsson 2001 [DIRS 154669], Attachment 9, pp. 57 to 74.



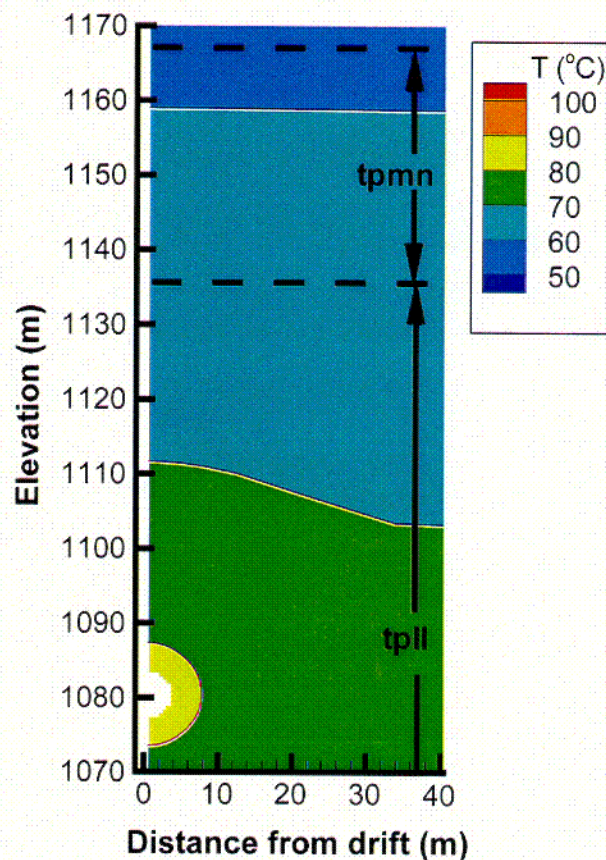
Lower-Temperature Case

154_0490a.ai

Figure 4.3.7-13. Vertical Permeability Changes at 10 Years



Higher-Temperature Case



Lower-Temperature Case

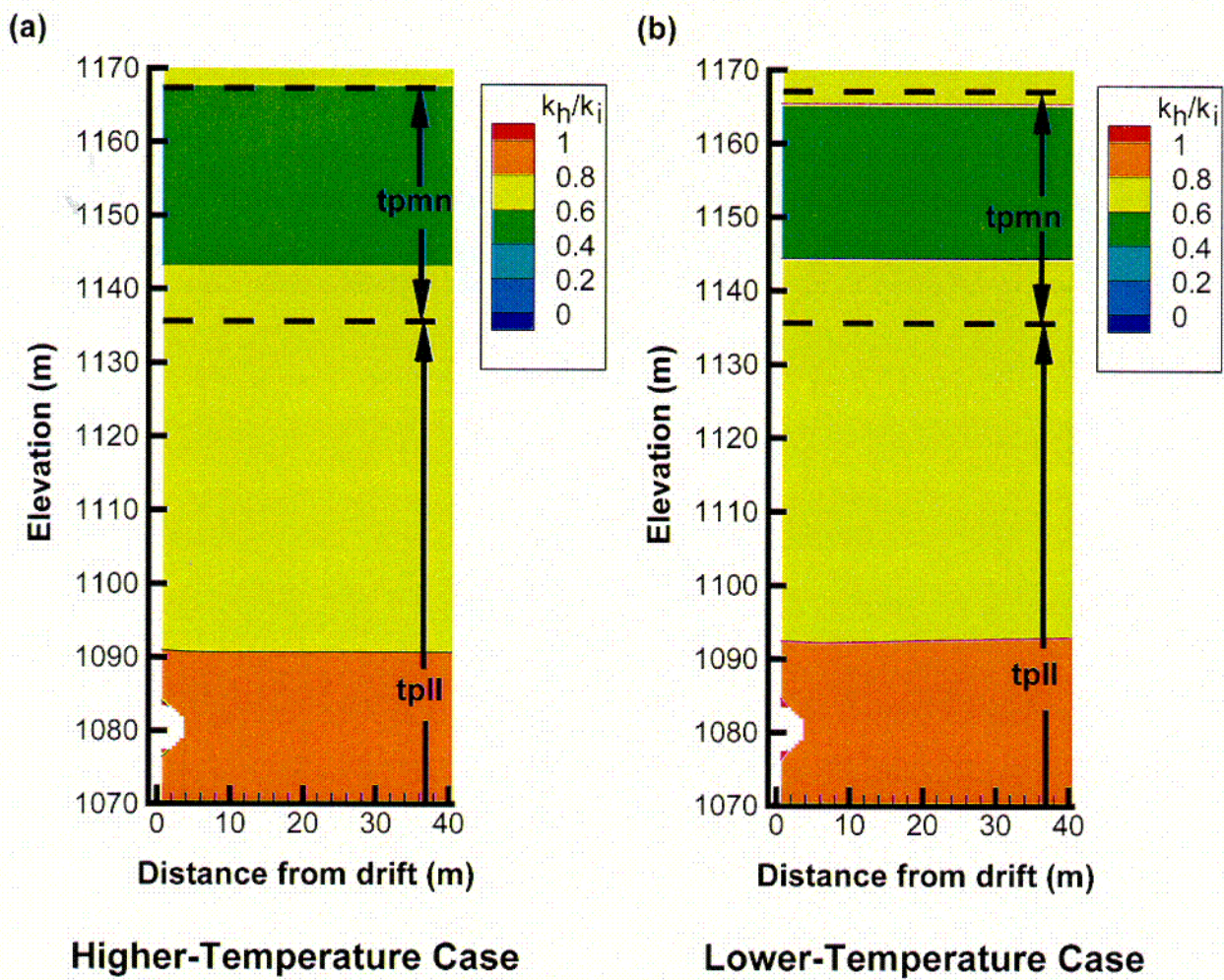
154_0491.ai

Source: Bodvarsson 2001 [DIRS 154669], Attachment 9, p. 69.

154_0491.ai

Figure 4.3.7-14. Temperature Distributions After 1,000 Years

C 35

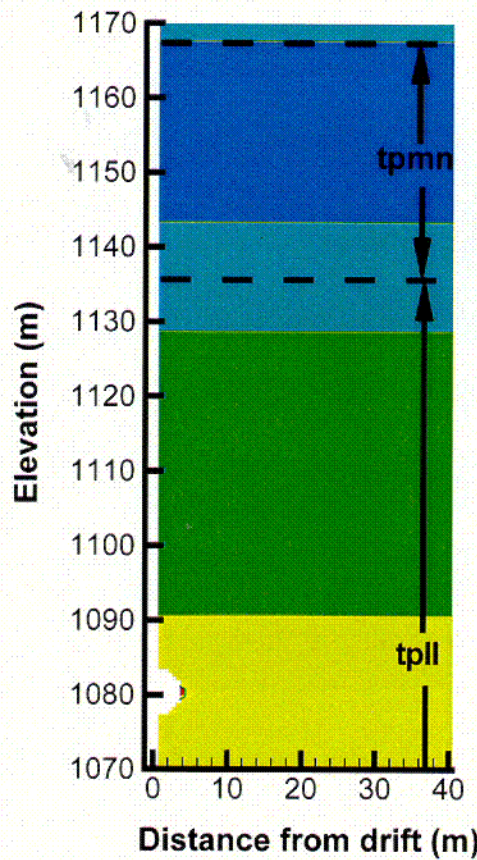


154_0492.ai

Source: Bodvarsson 2001 [DIRS 154669], Attachment 9, pp. 55 to 76.

154_0492.ai

Figure 4.3.7-15. Horizontal Permeability Changes at 1,000 Years

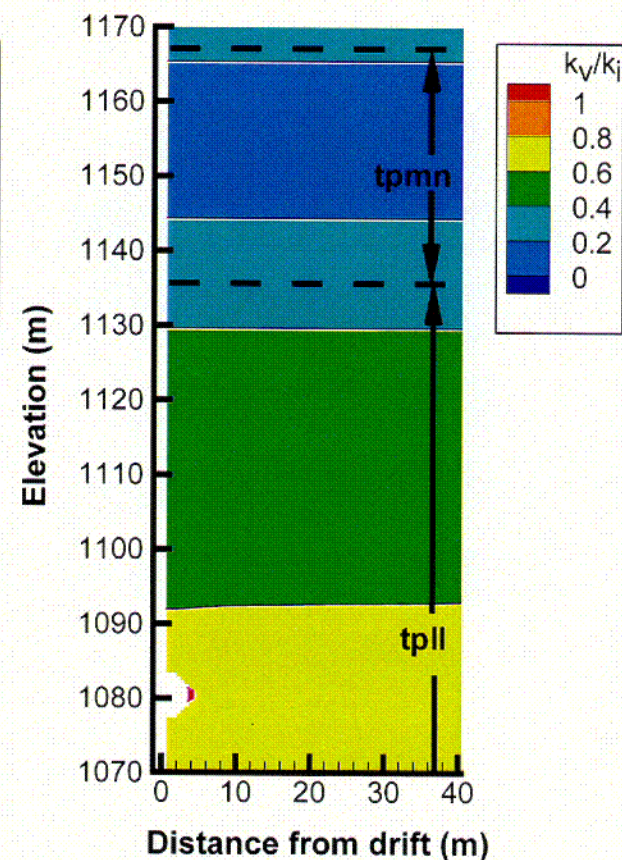


Higher-Temperature Case

154_0493.ai

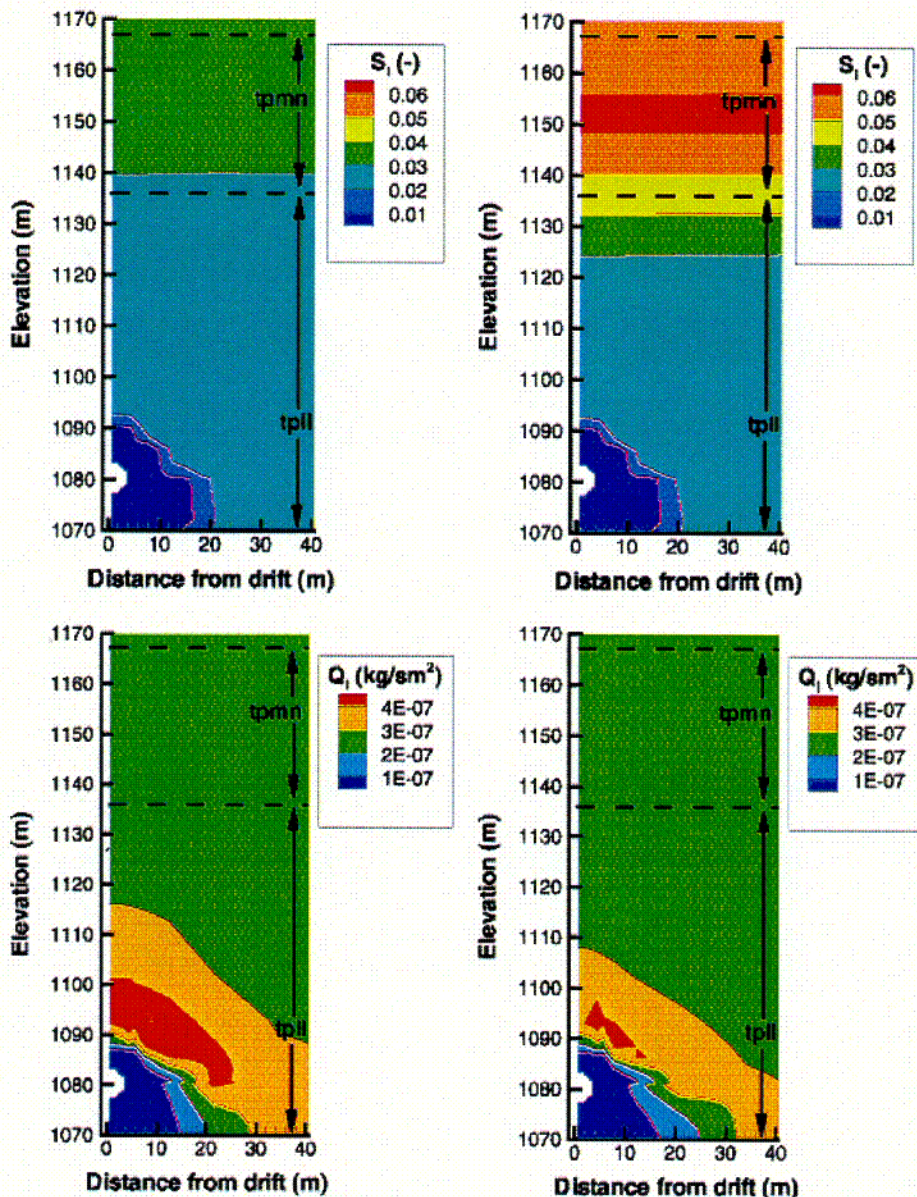
Source: Bodvarsson 2001 [DIRS 154669], Attachment 9, p. 70.

Figure 4.3.7-16. Vertical Permeability Changes at 1,000 Years



Lower-Temperature Case

154_0493.ai



154_0188.ai

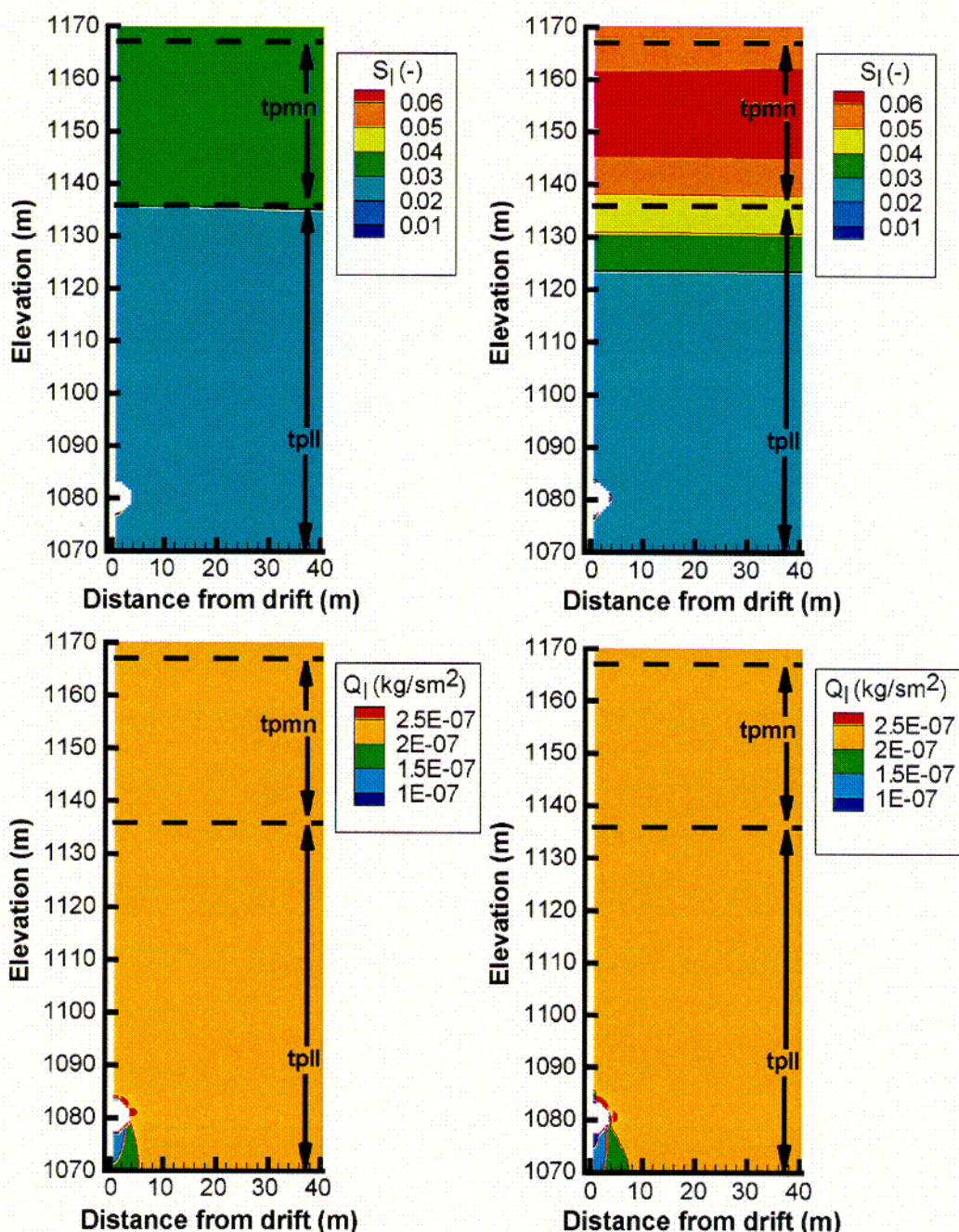
154_0188.ai

Source: Bodvarsson 2001 [DIRS 154669], Attachment 9, pp. 55 to 76.

NOTE: Comparison of results for saturation (upper panels) and percolation flux (lower panels) with thermal-hydrologic-mechanical processes (right) and purely thermal-hydrologic processes (left).

Figure 4.3.7-17. Distribution of Saturation and Percolation Flux for Thermal-Hydrologic-Mechanical and Thermal-Hydrologic Processes for the Higher-Temperature Case

C 38



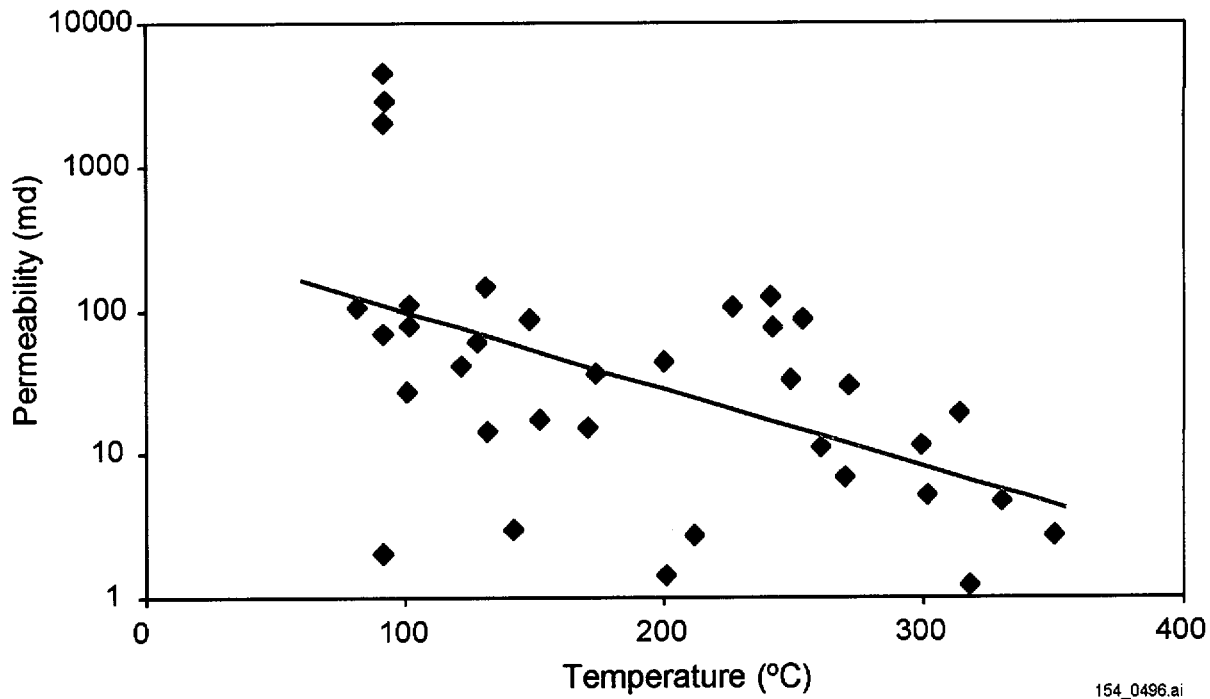
154_0495.ai

Source: Bodvarsson 2001 [DIRS 154669], Attachment 9, pp. 55 to 76.

NOTE: Results for the lower-temperature case. Comparison of results for saturation (upper panels) and percolation flux (lower panels) with thermal-hydrologic-mechanical processes (right) and purely thermal-hydrologic processes (left).

Figure 4.3.7-18. Distribution of Saturation (S_1) and Percolation Flux (Q_1) for Thermal-Hydrologic-Mechanical and Thermal-Hydrologic Processes for the Lower-Temperature Case

C39



154_0496.ai

Source: Based upon a survey by Björnsson and Bodvarsson 1990 [DIRS 154606]. Fit of the line from Bodvarsson 2001 [DIRS 154669], Attachment 4, p. 36.

Figure 4.3.7-19. Correlation Between Permeability and Temperature for Worldwide Geothermal Reservoir

INTENTIONALLY LEFT BLANK